Double parton scattering of weak gauge boson productions at the 13 TeV and 100 TeV proton-proton colliders

Qing-Hong Cao,[1,2,3,*] Yandong Liu,[1,†] Ke-Pan Xie,[1,‡] and Bin Yan[1,4,§]

[1]*Department of Physics and State Key Laboratory of Nuclear Physics and Technology, Peking University, Beijing 100871, China*
[2]*Collaborative Innovation Center of Quantum Matter, Beijing 100871, China*
[3]*Center for High Energy Physics, Peking University, Beijing 100871, China*
[4]*Department of Physics and Astronomy, Michigan State University, East Lansing, Michigan 48824, USA*

We study double parton scattering (DPS) processes involving electroweak gauge bosons at the 13 and 100 TeV proton-proton colliders. Specifically, we focus on three DPS channels: W-boson plus two jets ($W \otimes jj$), Z-boson plus two jets ($Z \otimes jj$), and same-sign W pair production ($W^\pm \otimes W^\pm$). We demonstrate that the $Z \otimes jj$ process, which has not received much attention, is the best channel for measuring the effective cross section $\sigma_{\rm eff}$. The accuracy of the $\sigma_{\rm eff}$ measurement in the three DPS channels, especially the $W^\pm \otimes W^\pm$ production, is significantly improved at the 100 TeV colliders. We advocate that combined analysis of the three DPS channels could test the universality of the effective cross section $\sigma_{\rm eff}$.

I. INTRODUCTION

The precise measurement of multiple parton interactions (MPI) is very important to improve our understanding of protons. In such a process, two or more short distance subprocesses occur in one given hadronic interaction. The correlations and distributions of multiple partons within a proton relate directly to the transverse spatial structure of the proton, but those effects are highly suppressed by the momentum transfer of hard scattering. A typical MPI at low scales is the double parton scattering (DPS), in which two pairs of partons participate in hard interactions in a single proton-proton collision, as illustrated in Fig. 1(a). As the simplest MPI process, DPS is different from the standard picture of the hadron-hadron collision in which one parton from each proton partakes in the hard scattering named as single parton scattering (SPS); see Fig. 1(b).

The cross section of a DPS process that contains two subprocesses A and B (denoted as $A \otimes B$) can be estimated as follows,

$$\sigma^{\rm DPS}_{A\otimes B} \approx \frac{1}{1+\delta_{AB}} \frac{\sigma^{\rm SPS}_A \otimes \sigma^{\rm SPS}_B}{\sigma_{\rm eff}}, \qquad (1)$$

where $\sigma_{\rm eff}$ is an effective cross section (~ 15 mb) that reflects the structure of the proton, and the symmetry factor δ_{AB} is introduced to avoid double counting, which is 1 for $A = B$ and 0 otherwise. $\sigma^{\rm SPS}_{A(B)}$ is the SPS cross section of subprocess $A(B)$, respectively. Given the large value of $\sigma_{\rm eff}$, it is usually expected that the effects of DPS are negligible or described in the parametrization of underlying events. However, the cross section of DPS can be sizably enhanced with increasing collider energy $\sqrt{s}$ if the subprocesses involve the sea quark or gluon in the initial state as the parton distribution function (PDF) of both sea quarks and gluons grows dramatically in the small x region. Therefore, at high-energy colliders, some of the DPS processes could yield enough signal events to be discovered. For the search
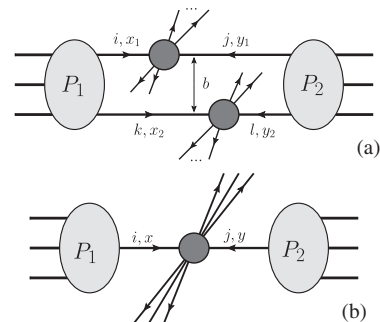
*qinghongcao@pku.edu.cn
†ydliu@pku.edu.cn
‡kpxie@pku.edu.cn
§yanbin1@msu.edu

FIG. 1. Pictorial illustration of double parton scattering (a) and single parton scattering (b).

TABLE I.   The cross section of the SPS processes of interest to us at the 13 TeV LHC and at the 100 TeV SppC/FCC-hh.

SPS Process	$pp \to jj$	$pp \to W$	$pp \to Z$
13 TeV	$\sim 10^8$ pb	$\sim 10^5$ pb	$\sim 10^4$ pb
100 TeV	$\sim 10^9$ pb	$\sim 10^6$ pb	$\sim 10^5$ pb

of new physics beyond the standard model (SM), the DPS processes can also be considerable backgrounds.

Owing to the unprecedented energy of the LHC, one expects to measure the model parameter σ_{eff} precisely through various DPS processes. That would shed light on MPI in hadron collisions; for example, there are a few open questions concerning DPS:

(1) how well can one measure σ_{eff} in hadron collisions?
(2) does σ_{eff} vary with colliding energies?
(3) is σ_{eff} universal for different DPS processes?

In this paper, we investigate then these problems at the 13 TeV LHC and also at a future hadron collider with a center of mass energy of 100 TeV, e.g. SppC [1] and FCC-hh [2]. In order to overcome the huge suppression of σ_{eff}, one should consider those DPS processes involving two sizable SPS subprocesses. Table I displays the cross sections of three SPS processes of interest to us. The jets in the dijet (jj)

production are required to satisfy the kinematic cuts of $p_T^j > 25$ GeV, $|\eta^j| < 5$ and $\Delta R_{jj} \geq 0.4$, where p_T and η denote the transverse momentum and rapidity, respectively, and $\Delta R_{mn} \equiv \sqrt{(\eta^m - \eta^n)^2 + (\phi^m - \phi^n)^2}$ represents the angular distance between the object m and n with ϕ being the azimuthal angle. Combining any two SPS processes in the list might yield a sizable DPS process.

Among the possibilities, $jj \otimes jj$ provides the largest cross section of DPS. Indeed, the four jets final state is a good channel to measure the DPS [3–7], but triggering the jets is challenging in high-energy hadron collisions. In contrast, the $W \otimes jj$ and $Z \otimes jj$ processes exhibit charged leptons in the final state and can be easily detected [8–10]. The pure electroweak processes, $W^\pm \otimes W^\mp$ or $W^\pm \otimes Z$, have sizable production rates, but it is challenging to extract them from the enormous SPS diboson backgrounds. However, the same-sign $W^\pm \otimes W^\pm$ channel has rather low SM backgrounds and is promising [11–14]. In addition, the production rate of quarkoniums, e.g. J/ψ, also has the potential to be a subprocess of DPS, and it has been studied both theoretically [15–23] and experimentally [24–30]. The precision calculations of SPS J/ψ associated production processes have been carried out recently [31–35] to refine the σ_{eff} extraction. Table II shows the effective

TABLE II.   Recent σ_{eff} measurements by different experiments and energies.

DPS channel	σ_{eff} (mb)	Collaboration	Collider	Luminosity
$jj \otimes jj$	$12.1^{+10.7}_{-5.4}$ $14.9^{+2.6}_{-3.1}$	CDF [4]	1.8 TeV Tevatron	325 nb^{-1}
$J/\Psi \otimes D$	$17.6^{+3.1}_{-4.0}$ $12.8^{+2.6}_{-3.2}$ $18.0^{+4.8}_{-5.5}$	LHCb [24]	7 TeV LHC	355 pb^{-1}
$W \otimes jj$	$15.0^{+5.8}_{-4.2}$	ATLAS [10]	7 TeV LHC	36 pb^{-1}
$W^\pm \otimes W^\pm$	>5.91	CMS [11]	8 TeV LHC	19.7 fb^{-1}
$W \otimes jj$	$20.7^{+6.6}_{-6.6}$	CMS [9]	7 TeV LHC	5 fb^{-1}
$\gamma j \otimes jj$	$12.7^{+1.3}_{-1.3}$ $14.5^{+3.3}_{-5.3}$	D0 [36]	1.96 TeV Tevatron	8.1 fb^{-1}
$jj \otimes jj$	$16.1^{+6.4}_{-7.0}$	ATLAS [5]	7 TeVLHC	37.3 pb^{-1}
$\gamma\gamma \otimes jj$	$19.3^{+7.9}_{-7.9}$	D0 [37]	1.96 TeV Tevatron	8.7 fb^{-1}
$J/\Psi \otimes J/\Psi$	$4.80^{+2.55}_{-2.55}$ $14.4^{+4.9}_{-4.9}$	D0 [25]	1.96 TeV Tevatron	8.1 fb^{-1}
$J/\Psi \otimes J/\Psi$	$9.2^{+3.9}_{-3.9}$ $11.3^{+1.5}_{-1.5}$	LHCb [26]	13 TeV LHC	5 fb^{-1}
$J/\Psi \otimes J/\Psi$	$6.3^{+1.9}_{-1.9}$	ATLAS [27]	8 TeV LHC	11.4 fb^{-1}
$Z \otimes J/\Psi$	>5.3	ATLAS [29]	8 TeV LHC	20.3 fb^{-1}
$\Upsilon \otimes J/\Psi$	$2.2^{+1.1}_{-1.1}$	D0 [30]	1.96 TeV Tevatron	8.1 fb^{-1}

cross section σ_{eff} measured by different experiments and energies. The results do not converge into a single value and have large errors. The average σ_{eff} is approximately 15 mb. In this work, we will study the $W \otimes jj$, $Z \otimes jj$, and $W^{\pm} \otimes W^{\pm}$ channels and explore the potential of measuring $\sigma_{\text{eff}} \sim 10$–20 mb at the 13 and 100 TeV colliders.

The paper is organized as follows. We introduce the framework and various double parton models in Sec. II. A comparison of two double parton models is presented in Sec. III. We use the simply factorized model to investigate the phenomenologies of the three DPS processes in Secs. IV–VI. Finally, we present a combined analysis of the three DPS channels and conclude in Sec. VII.

II. FRAMEWORK

According to factorization theorem [38], the inclusive cross section of SPS is expressed as

$$\sigma_Y^{\text{SPS}} = \sum_{ij} \int dx dy f_i(x, \mu_F) f_j(y, \mu_F) \hat{\sigma}_{ij}^Y(x, y), \quad (2)$$

where $\hat{\sigma}_{ij}^Y$ is the inclusive cross section of parton scattering $ij \to Y$, and the parton distribution functions (PDF) $f_i(x, \mu_F)$ represent the probability of finding a parton i with a momentum fraction x and scale μ_F in a proton. The physical meaning of this equation can be read clearly in Fig. 1(b). Unlike SPS, however, the cross section of DPS does not have a well-proved expression yet. In general, the DPS cross section can be written down as [39,40]

$$\sigma_{A \otimes B}^{\text{DPS}} = \frac{1}{1 + \delta_{AB}} \sum_{ijkl} \int dx_1 dy_1 dx_2 dy_2 d^2 b$$
$$\times \Gamma_{ik}(x_1, x_2, \mu_F, \mu_F'; b) \Gamma_{jl}(y_1, y_2, \mu_F, \mu_F'; b)$$
$$\times \hat{\sigma}_{ij}^A(x_1, y_1) \hat{\sigma}_{kl}^B(x_2, y_2), \quad (3)$$

where $\Gamma_{ik}(x_1, x_2, \mu_F, \mu_F'; b)$ represents the probability of finding two partons i (with momentum fraction x_1 and scale μ_F) and k (with momentum fraction x_2 and scale μ_F') with a transverse distance separation b. $\Gamma_{jl}(y_1, y_2, \mu_F, \mu_F'; b)$ has a similar meaning. In addition, $\hat{\sigma}_{ij}^A$ and $\hat{\sigma}_{kl}^B$ are the subprocess cross sections for inclusive $ij \to A$ and $kl \to B$, respectively. See Fig. 1(a) for a pictorial illustration. In general, the longitudinal momentum fractions (the x's and y's) and the transverse separation b are correlated in DPS, and can be studied in a light-front quark model approach [41–43]. Ignoring the transverse correlation of partons, Γ_{ik} can be factorized as [39,40]

$$\Gamma_{ik}(x_1, x_2, \mu_F, \mu_F'; b) = D_{ik}(x_1, x_2, \mu_F, \mu_F') F(b), \quad (4)$$

where the double PDF (dPDF) D_{ik} describes the longitudinal structure of double partons while $F(b)$ represents the effective transverse overlap area of partonic interactions

that produces the characteristic phenomena of the DPS process. The $F(b)$ is usually assumed to be the same for all parton pairs involved in the DPS process of interest. Integrating over the distance b yields the *master formula* in our study,

$$\sigma_{A \otimes B}^{\text{DPS}} = \frac{1}{1 + \delta_{AB}} \frac{1}{\sigma_{\text{eff}}} \sum_{ijkl}$$
$$\times \int dx_1 dy_1 dx_2 dy_2 D_{ik}(x_1, x_2, \mu_F, \mu_F')$$
$$\times D_{jl}(y_1, y_2, \mu_F, \mu_F') \hat{\sigma}_{ij}^A(x_1, y_1) \hat{\sigma}_{kl}^B(x_2, y_2), \quad (5)$$

where the effective cross section,

$$\sigma_{\text{eff}}^{-1} \equiv \int d^2 b (F(b))^2, \quad (6)$$

is sensitive to the transverse size of incoming protons. Its value is difficult to derive from the parton model assumptions and has to be determined from experiments.

Although the dPDF should be measured in experiments, one often assumes it can be built up from the single parton PDFs. Various construction approaches have been proposed [40,44–47]. In general, the dPDF can be written as

$$D_{ik}(x_1, x_2, \mu_F, \mu_F') = f_i(x_1, \mu_F) f_k(x_2, \mu_F') \rho_{ik}(x_1, x_2),$$

where ρ_{ik} describes the correlation between the two partons. A simple model is to ignore longitudinal momentum correlations of the two parton and only demands their momentum sum less than the momentum of their mother proton, i.e.

$$\rho_{ik}(x_1, x_2) = \theta(1 - x_1 - x_2). \quad (7)$$

Such an approximation is typically justified at low x values on the grounds that the population of partons is large at these values. Making use of the typically small $x_{1,2}$ and $y_{1,2}$ in hard scattering, one can drop this constraint and obtain the approximate expression Eq. (1). We name it as "simply factorized" (SF) dPDF, which is widely used both in theoretical [39,48–57] and experimental studies [4–13,24,36,37]. Although those experiments cover various processes such as $jj \otimes jj$ [3–7], $W^{\pm} \otimes jj$ [8–10], $W^{\pm} \otimes W^{\pm}$ [11–14], J/ψ meson associated processes [24,27,29,30], $\gamma j \otimes jj$ [36] and $\gamma \gamma \otimes jj$ [37], they all give $\sigma_{\text{eff}} \sim \mathcal{O}(10)$ mb, and most of them give ∼15 mb. This fact gives strong evidence to the validity of the SF model and the universality of σ_{eff}.

The SF model, simple and supported by experimental data, ignores the longitudinal correlation between the two subprocesses. In a theoretical perspective, the SF model does not obey the dPDF sum rules and evolution equations. Reference [40] proposes an improved dPDF named as GS09 by assuming $\mu_F = \mu_F'$ and setting

$$\rho_{ik}(x_1, x_2) = (1 - x_1 - x_2)^2 (1 - x_1)^{-2-\alpha_i}(1 - x_2)^{-2-\alpha_k},$$
$$(8)$$

where $\alpha_i = 0$ for sea partons and 0.5 for valence partons. Nevertheless, different double parton models give nearly the same results in the small x region where the parton correlation is negligible [40]. A comparable study that applies a completely correlated, unfactorized model for the dPDFs (such as the one of Ref. [41]) would be useful to study whether the LHC can test the validity of the factorized assumption. We will investigate it in the future.

III. SIMPLE FACTORIZED DPDF VERSUS GS09 DPDF

In this study, we use the SF model specified in Eq. (7) to study the DPS, but before moving to the detailed phenomenological study, we compare different double parton models in the next section.

The comparison of the SF and GS09 dPDFs has been investigated in the $Z \otimes$ jets channel [48] and the $W \otimes W$ channel [39]. It was shown that both the SF and GS09 dPDFs give rise to consistent cross sections within $\sim 10\%$ accuracy and, furthermore, the kinematics distributions of p_T, η and invariance mass are insensitive to the choice of dPDFs. Below we examine the difference of the two dPDFs in the $W \otimes jj$, $Z \otimes jj$, and $W^{\pm} \otimes W^{\pm}$ processes.

A. Parton luminosity

To compare these two kind of dPDFs, we should not only discuss the cross sections for some specific processes, but also study the parton luminosities. The parton luminosity is an important quantity to estimate the order-of-magnitude of hard process cross section in hadron collisions. In the SPS, it is defined as [58]

$$\frac{dL_{ij}}{d\tau} = \frac{1}{1 + \delta_{ij}} \int_{\tau}^{1} \frac{dx}{x} [f_i(x, \mu_F) f_j(\tau/x, \mu_F) + f_j(x, \mu_F) f_i(\tau/x, \mu_F)],$$
$$(9)$$

where the indices i and j label the incoming partons; see Fig. 1(b). The δ_{ij} symbol is used to avoid double counting. This definition is process independent and reflects the properties of PDF. In a DPS process depicted in Fig. 1(a), we define double parton luminosity as

$$\frac{dL_{ij,kl}}{d\tau_1 d\tau_2} = \frac{1}{1 + \delta_{ik}\delta_{jl}} \frac{1}{1 + \delta_{ij}} \frac{1}{1 + \delta_{kl}} \int_{\tau_1}^{1} \frac{dx_1}{x_1} \int_{\tau_2}^{1} \frac{dx_2}{x_2}$$
$$\times [D_{ik}(x_1, x_2, \mu_F) D_{jl}(\tau_1/x_1, \tau_2/x_2, \mu_F)$$
$$+ D_{jk}(x_1, x_2, \mu_F) D_{il}(\tau_1/x_1, \tau_2/x_2, \mu_F)$$
$$+ D_{il}(x_1, x_2, \mu_F) D_{jk}(\tau_1/x_1, \tau_2/x_2, \mu_F)$$
$$+ D_{jl}(x_1, x_2, \mu_F) D_{ik}(\tau_1/x_1, \tau_2/x_2, \mu_F)], \quad (10)$$

which, in the SF dPDF model, can be simplified as

$$\left(\frac{dL_{ij,kl}}{d\tau_1 d\tau_2}\right)_{\text{SF}} = \frac{1}{1 + \delta_{ik}\delta_{jl}} \frac{1}{1 + \delta_{ij}} \frac{1}{1 + \delta_{kl}}$$
$$\times \int_{\tau_1}^{1} \frac{dx_1}{x_1} \int_{\tau_2}^{1} \frac{dx_2}{x_2} \theta(1 - x_1 - x_2) \theta$$
$$\times (1 - \tau_1/x_1 - \tau_2/x_2)$$
$$\times [f_i(x_1, \mu_F) f_j(\tau_1/x_1, \mu_F) + (i \leftrightarrow j)]$$
$$\times [f_k(x_2, \mu_F) f_l(\tau_2/x_2, \mu_F) + (l \leftrightarrow k)].$$
$$(11)$$

We calculate the parton luminosities of both the GS09 and the SF dPDFs using Eqs. (10) and (11), respectively. In the available GS09 dPDF code, the single MSTW2008LO PDF sets [59] are used to realized Eq. (8), therefore, we use the same set of single PDF in the SF calculation. We then plot the contour of the parton luminosity ratio,

$$\left(\frac{dL_{ij,kl}}{d\tau_1 d\tau_2}\right)_{\text{GS09}} \bigg/ \left(\frac{dL_{ij,kl}}{d\tau_1 d\tau_2}\right)_{\text{SF}}, \quad (12)$$

in Fig. 2 for the three DPS processes: (a) $(u\bar{d} \to W^+) \otimes (gg \to jj)$, (b) $(u\bar{u} \to Z) \otimes (gg \to jj)$ and (c) $(u\bar{d} \to W^+) \otimes (u\bar{d} \to W^+)$. As shown in Sec. III C below, these parton

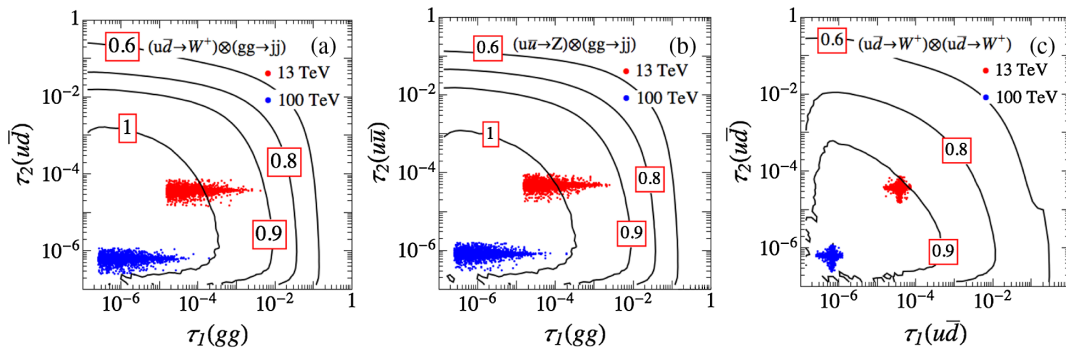

FIG. 2. The ratio of parton luminosities in the GS09 dPDF and SF dPDF: (a) $u\bar{d} \otimes gg \to W^+ \otimes jj$; (b) $u\bar{u} \otimes gg \to Z \otimes jj$; (c) $u\bar{d} \otimes u\bar{d} \to W^+ \otimes W^+$. The red (blue) points denote the ratio at the 13 (100) TeV colliders, respectively.
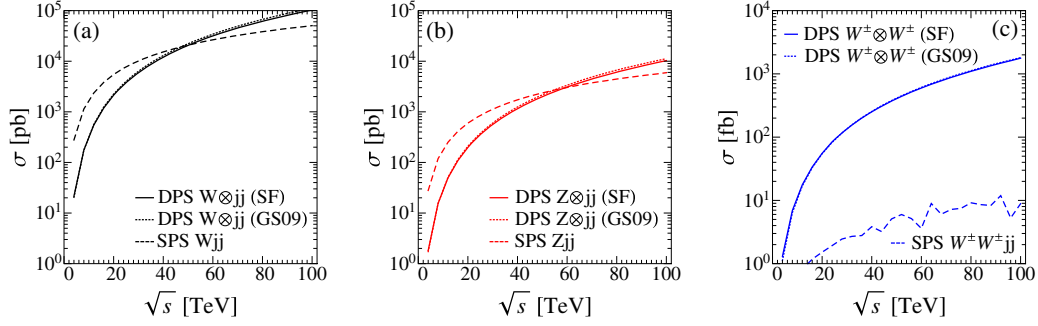
FIG. 3.   Cross sections of the DPS processes as a function of collider energy $\sqrt{s}$: (a) $W \otimes jj$, (b) $Z \otimes jj$, and (c) $W^{\pm} \otimes W^{\pm}$ productions. The solid and dotted curve represents the DPS production calculated with the SF and GS09 dPDF, respectively, while the dashed curve denotes the SPS production. The jets are required to pass the selection cuts shown in Eq. (13).

combinations dominate in the three DPS channels. The PDF scales are chosen as $m_W = 80.4$ GeV. Of course, the jets can also be produced from initial state quarks, but for a clear illustration, we consider only the dominant channel $gg \to jj$ in the comparison of parton luminosities. The red points denote the ratio at the 13 TeV LHC while the blue points represent the ratio at the 100 TeV SppC/FCC-hh.

The SF and GS09 dPDFs give rise to comparable parton luminosities in the region of small τ, say $\tau \sim 10^{-4}$. The difference between the two dPDFs becomes evident for $\tau \gtrsim 10^{-2}$ [40]. At a collider with the fixed center of mass energy, each individual scattering channel exhibits a typical τ value. For example, the gauge bosons mass provides a natural scale in the W-boson or Z-boson production, therefore, the τ value populates mainly around $m_{W,Z}^2/s$. It yields $\tau \sim 4 \times 10^{-5}$ at the 13 TeV LHC and $\tau \sim 10^{-6}$ at the 100 TeV SppC/FCC-hh. For the $gg \to jj$ production the scale depends on the p_T cuts imposed (which is 25 GeV in this study), making τ_{gg} distributes mostly in $(50 \text{ GeV})^2/s$. It yields a similar τ value as the W- or Z-boson production. As there is no resonance in the jj production, the τ value exhibit a long tail towards larger τ.

Figure 2 shows that the most of the luminosity ratios populates around $0.9 \sim 1.1$ for both the $W \otimes jj$ and $Z \otimes jj$ channel at the 13 TeV LHC, while the luminosity ratio of $W^{\pm} \otimes W^{\pm}$ channel is around 0.9. It implies that the $W^{\pm} \otimes W^{\pm}$ production can be used to study the difference between GS09 and SF dPDFs at the 13 TeV LHC. For example, Ref. [39] points out that the pseudorapidity asymmetry of charged leptons can be used to discriminate various dPDF sets efficiently.

B. Cross sections

Figure 3 displays the cross sections of the three DPS channels: (a) $W \otimes jj$ (black), (b) $Z \otimes jj$ (red), and (c) same-sign $W^{\pm} \otimes W^{\pm}$ (blue) productions as a function of colliding energy ($\sqrt{s}$). The solid curve represents the cross sections of the DPS channel calculated with the SF dPDF while the dotted curve evaluated with the GS09

dPDF. For comparison, we also plot the SPS background processes (dashed curve). In order to avoid the collinear singularity, all the jets in the $W \otimes jj$ and $Z \otimes jj$ productions are required to pass the selection cuts as follows:

$$p_T^j > 25 \text{ GeV}, \qquad |\eta^j| < 5, \qquad \Delta R_{jj} \geq 0.4. \qquad (13)$$

We notice that both the SF and GS09 dPDFs generate almost identical production rates in the three DPS channels; see the solid and dotted curves. The cross sections of $W \otimes jj$ and $Z \otimes jj$ productions increase rapidly with the collider energy and exceed the SPS cross section around $\sqrt{s} = 60$ TeV; see Figs. 3(a) and 3(b).

In the SPS, the same-sign W-boson pairs are produced in association with two extra jets. In order to mimic the DPS $W^{\pm} \otimes W^{\pm}$ production, the two additional jets in the SM SPS channel are required to escape detection, i.e. the extra jets satisfying Eq. (13) are vetoed. The jet-veto cut significantly suppresses the SPS production rate. As shown in Fig. 3(c), the SPS channel is about one order of magnitude smaller than the DPS channel after vetoing additional jets. Also, the cross section of the DPS $W^{\pm} \otimes W^{\pm}$ production increases dramatically with collider energy.

C. Fraction of double parton combinations

In the study of the parton luminosity ratio in Sec. III A, we only consider the parton pairs in one proton that play the leading role in the DPS channels. It is interesting to ask how often a parton pair contributes in the DPS channels of interest to us. We separate the $W^+ \otimes jj$ and $W^- \otimes jj$ channels, as well as $W^+ \otimes W^+$ and $W^- \otimes W^-$ channels, in order to see the difference between valence quarks and sea quarks.

Electroweak gauge bosons see quarks but not gluons in the proton. To produce the $W^{\pm}$ or Z boson, each proton need provide at least one quark. For example, the $W^+ \otimes jj$ channel requires the initial state parton combinations as follows:
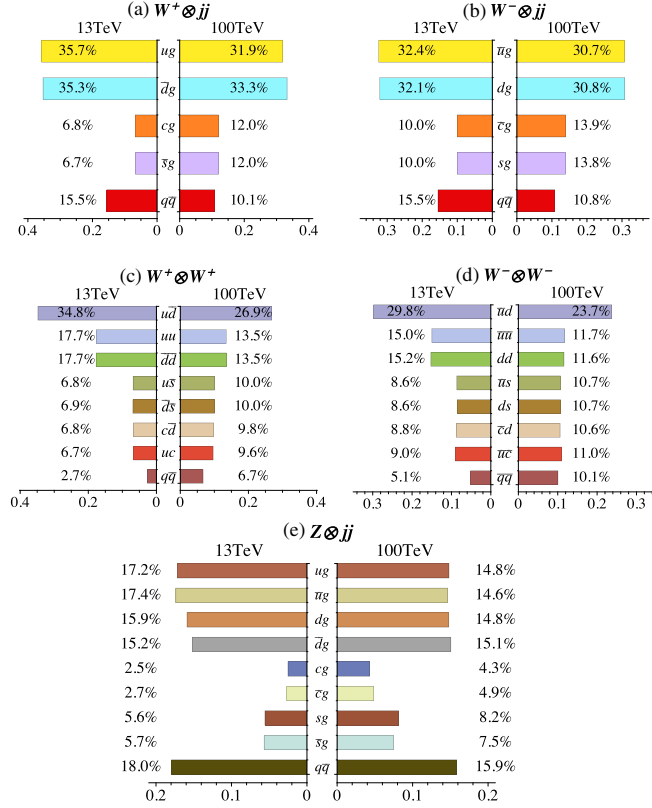
FIG. 4. The fraction of double parton combinations in the DPS processes: (a) $W^+ \otimes jj$, (b) $W^- \otimes jj$, (c) $W^+ \otimes W^+$, (d) $W^- \otimes W^-$ and (e) $Z \otimes jj$.

$$(ug) \otimes (\bar{d}g), (uq) \otimes (\bar{d}g), ug \otimes (\bar{d}q), (uq) \otimes (\bar{d}q'),$$
$$(cg) \otimes (\bar{s}g), (cq) \otimes (\bar{s}g), cg \otimes (\bar{s}q), (cq) \otimes (\bar{s}q'), \cdots$$

where $q(q') = u, d, c, s, b$. We generate ten thousand events in the $W^+ \otimes jj$ channel and count the number of events with a specific parton i and j pair (N_{ij}) in one proton to obtain the fraction ϵ_{ij},

$$\epsilon_{ij} = \frac{N_{ij}}{N_{\text{total}}}. \tag{14}$$

Figure 4(a) displays the fraction of parton pairs in one proton at the 13 and 100 TeV colliders. As expected, the ug pairs and $\bar{d}g$ pairs dominate the DPS process, e.g. $\epsilon_{ug} \simeq \epsilon_{\bar{d}g} \sim 35\%$ at the LHC. The subsidiary contribution is from either the cg or $\bar{s}g$ pair, which yields $\epsilon_{cg} \simeq \epsilon_{\bar{s}g} \sim 6.8\%$. A pair of quarks in one proton only occurs about 1% of the total time, but summing over all the possible quark pairs gives rise to 15.5%. We denote the sum of all quark pairs as $q\bar{q}$. Hence, the $W^+ \otimes jj$ channel is dominated by the initial state parton configure of a pair of quark and gluon from one proton and another pair of quark and gluon from the other proton, i.e. $(qg) \otimes (\bar{q}'g)$. The 100 TeV collider probes a much smaller x at which the gluon and sea quark PDF's

increase dramatically. Therefore, the fraction of ug pairs decreases slightly to $\epsilon_{ug} = 32\%$, but the fractions of cg and $\bar{s}g$ pairs are almost doubled. A similar result is observed in the $W^- \otimes jj$ channel; see Fig. 4(b).

The $W^+ \otimes W^+$ channel has two gauge bosons and, thus, demands four quarks in the initial state, which are listed as follows:

$$(u\bar{d}) \otimes (u\bar{d}), (uu) \otimes (\bar{d}\bar{d}), u\bar{s} \otimes (\bar{d}c), (uc) \otimes (\bar{d}\bar{s}), ...$$

Figure 4(c) shows the fractions of quark pairs listed above. The $u\bar{d}$ pair is the leading double partons in the $W^+ \otimes W^+$ production, $\epsilon_{u\bar{d}} \simeq 35\%$. The uu and $\bar{d}\bar{d}$ pairs are the second double partons, $\epsilon_{uu,\bar{d}\bar{d}} \simeq 18\%$. Other quark pairs ($u\bar{s}$, $\bar{d}\bar{s}$, $c\bar{d}$ and uc) contribute almost equally, $\epsilon_{u\bar{s},\bar{d}\bar{s},c\bar{d},uc} \simeq 7\%$. The rest of the quark pairs not listed above only contribute 2.7% in total. Increasing the collider energy enhances the fraction of sea quark pairs and reduces the share of $u\bar{d}$ pairs. The pattern is also applied to the $W^- \otimes W^-$ channel; see Fig. 4(d).

The $Z \otimes jj$ channel is complicated as it involves more double parton combinations, e.g.

$$ug, \bar{u}g, dg, \bar{d}g, cg, \bar{c}g, sg, \bar{s}g, ... \tag{15}$$

Figure 4(e) displays the fractions of parton pairs. Again, we use the $q\bar{q}$ to denote the sum of all quark pairs. We note that about 82% of parton pairs are a combination of quark and gluon, which is similar to the $W \otimes jj$ channel.

We emphasize that the σ_{eff}'s measured in the $W \otimes jj$ and $Z \otimes jj$ channels are sensitive to the double parton configuration of $(qg) \otimes (\bar{q}'g)$ while the one measured in the $W^\pm \otimes W^\pm$ channel is sensitive to the configuration of $(q\bar{q}') \otimes (q\bar{q}')$. Therefore, measuring σ_{eff} from various DPS channels involving weak bosons can check the σ_{eff} universality. Were different σ_{eff}'s reported in various DPS processes at the LHC or future colliders, the difference might shed lights on the double parton transverse correlations.

D. Rapidity difference

Another important difference between the 13 and 100 TeV hadron colliders is the detector coverage of the pseudorapidity of final state particles. It has a significant impact on the kinematics cuts used to disentangle the signal out of the SM backgrounds. At the 13 TeV LHC, the detector can well detect jets or leptons in the centra region, say $|\eta| < 2.5$ for leptons and $|\eta| < 5$ for jets [60,61]. At the 100 TeV hadron colliders, the final state particles are often highly boosted to appear in the very forward region of the detector and thus exhibit large rapidities [2]. Below we examine the rapidity coverage of charged leptons and jets in the three DPS channels at the 13 and 100 TeV hadron colliders. That guides us to decide which rapidity cut to be
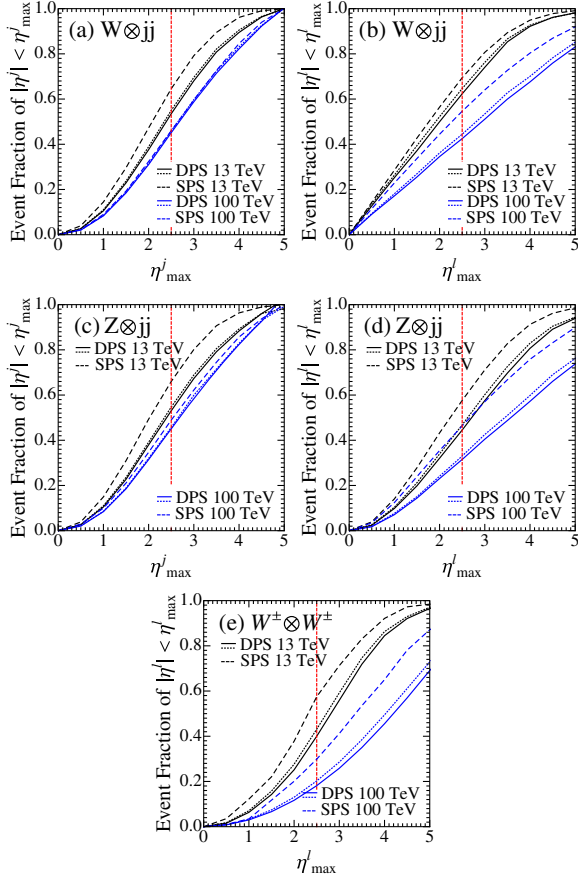
FIG. 5. Cross section fraction as a function of maximal pseudorapidity of jets and leptons: (a) $W \otimes jj$, (b) $Z \otimes jj$ and (c) same sign $W^{\pm} \otimes W^{\pm}$ process. The solid (dotted) curve represents the DPS production calculated with SF (GS09) dPDF, while the dashed curve represents the SPS channel, respectively. The cuts are listed in text.

used at the 100 TeV colliders. Also, a comparison between the SPS and DPS processes is made.

Figure 5 shows the event fraction as a function of maximal pseudorapidity cut imposed on the charged leptons and jets in the final state of the three DPS channels and the corresponding SPS backgrounds. The event fraction of object i is defined as

$$\frac{1}{\sigma_{\text{total}}} \int_{-\eta^i_{\text{max}}}^{\eta^i_{\text{max}}} d\eta^i \frac{d\sigma}{d\eta^i}, \qquad (16)$$

where η^i_{max} is the maximal pseudorapidity cut imposed on the object i. In order to avoid the collinear divergence, we require all the jets in the $W \otimes jj$ and $Z \otimes jj$ channels to pass the selection cut as follows:

$$p_T^j > 25 \text{ GeV at the 13 TeV LHC};$$
$$p_T^j > 50 \text{ GeV at the 100 TeV colliders.} \qquad (17)$$

We also veto the jets satisfying the above condition in the $W^{\pm}W^{\pm}jj$ SPS process. No p_T cut is imposed on leptons.

Figures 5(a) and 5(b) display the event fraction of η_{max} of the jets and charged leptons in the $W \otimes jj$ channel, respectively. First, the SF (solid) and GS09 (dotted) dPDFs give rise to almost the same event fraction distribution. Second, at the 100 TeV SppC/FCC-hh, both leptons and jets are distributed more in large η ranges. For example, there are less than $\sim 40\%$ of the jets lying in the range of $|\eta^{\ell}| < 2.5$; see the intersection points of the red dashed vertical lines and the blue lines. In order to collect as many DPS events as possible, we have to cover a lager η range at the 100 TeV collider. In the study, we assume the lepton trigger covers the region $|\eta^{\ell}| < 5$ at the SppC/FCC-hh [62].

IV. $W \otimes jj$ CHANNEL

Figure 6 shows the pictorial illustration of (a) the DPS $W \otimes jj$ channel and (b) the SPS Wjj background. The $W \otimes jj$ channel strikes a balance between event triggering and production rate. On one hand, the charged lepton from the W-boson decay provides a nice trigger of the signal events; on the other hand, the jj subprocess give rise to a large cross section. Therefore, the channel has been searched experimentally for a long time, e.g. by the CMS Collaboration [8,9] and by the ATLAS Collaboration at the 7 TeV LHC [10]. Also, it has been studied theoretically both at the Tevatron [52] and the LHC [50,53]. In this section, we first discuss various kinematic distributions and then make a hadron level simulation to explore the potential of measuring σ_{eff} at the 13 TeV LHC and 100 TeV SppC/FCC-hh.

A. Kinematics distributions

We generate the subprocess $pp \rightarrow W \rightarrow l\nu_l$ (merged with $pp \rightarrow Wj$) and the subprocess $pp \rightarrow jj$ (merged with $pp \rightarrow jjj$) with MadGraph 5 [63], and then interface with Pythia 6 [64] and Delphes 3 [65] for parton shower and detector simulations. When generating the signal in MadGraph, we impose loose cuts on jets at the generator level as follows:

$$p_T^j \geq 10 \text{ GeV}, \qquad |\eta^j| < 5. \qquad (18)$$

to avoid the collinear divergence in QCD radiations, while no cut is added to the leptons. We further demand a set of
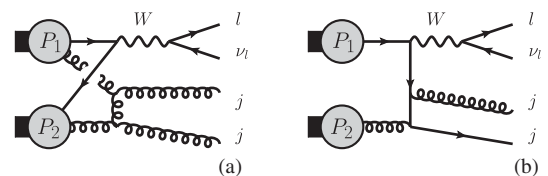

FIG. 6. Typical Feynman diagrams of DPS $W \otimes jj$ (a) and SPS Wjj (b).

loose conditions on the reconstruction of jets and leptons in the DELPHES package as follows,

$$p_T^\ell > 10 \text{ GeV}, \qquad |\eta^\ell| < 2.5(5),$$
$$p_T^j > 20 \text{ GeV}, \qquad |\eta^j| < 5, \qquad (19)$$

at the 13 (100) TeV colliders, respectively. Next, we randomly combine the events of these two subprocesses to get the $W \otimes jj$ DPS events. At hadron colliders, massive particles are mainly produced near threshold, thus the partons participating the subprocess of W-boson production typically have a typical momentum fraction $\langle x \rangle$ of the order of $\langle x \rangle \sim m_W/\sqrt{s} \sim 10^{-3}$ at the 13 TeV LHC and $\sim 10^{-4}$ at the 100 TeV SppC/FCC-hh; on the other hand, for the subprocess of jj production, the momentum fraction depends on the p_T^j cut, which is 10 GeV at the generator level, making $\langle x \rangle \sim (10 \text{ GeV})/\sqrt{s} \sim 10^{-5}$ or less. As a result, the combined events can hardly break the PDF integration condition in Eq. (5). To wit, even though being combined randomly without any additional constraints, the DPS events will satisfy $x_1 + x_2 \leq 1$ and $y_1 + y_2 \leq 1$ automatically. The fact has been checked: we randomly combine 10^6 events and find that none of them breaks the above conditions.

Additionally, we generate the DPS $W \otimes jj$ events at the parton-level with a homemade event generator which can handle two independent SPS processes simultaneously. We examine various parton-level distributions of final state particles and find good agreements with those distributions obtained by randomly combining two independent subprocesses generated by MADGRAPH.

The DPS $W \otimes jj$ channel contains two independent hard subprocesses such that the final state particles build up two uncorrelated subsystems. On the other hand, those final state particles of the dominant SM background channel, the SPS Wjj production, are correlated. The difference can be used to discriminate the DPS channel from the SPS background. We plot the kinematic distributions for DPS and SPS events after DELPHES reconstruction. As shown in Figs. 7(a) and 7(b), the p_T distribution of the charged lepton in the DPS event (black curve) has a Jacobi peak around $m_W/2$ as the charged leptons are from an on-shell W-boson that exhibits small p_T [66,67]. In the SPS background (blue curve), the two jets are produced in association with the W-boson. As we demand both jets carrying hard p_T's, the W-boson exhibits a large p_T to balance the two jets. It thus results in a harder p_T distribution of charged leptons; see the blue curves in Figs. 7(a) and 7(b).

Figures 7(c) and 7(d) display the p_T distributions of the leading p_T jet. The jets in the SPS background are much harder than those jets in the DPS channel. The jet p_T spectrum of the DPS channel peaks around the cut threshold specified in Eq. (17) and drops rapidly with p_T. On the contrary, the leading jet of the SPS channel tends to balance
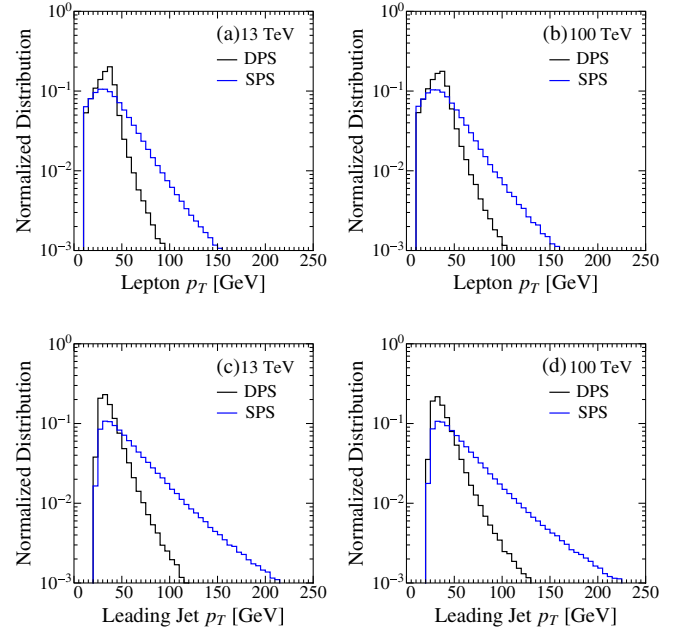

FIG. 7. The p_T distribution of charged lepton (a, b) and leading jet (c, d) in the $W \otimes jj$ channel at the 13 TeV LHC and the 100 TeV SppC/FCC-hh.

the W-boson such that it has a long tail in the large p_T region. Therefore, in order to extract the DPS signal out of the SPS background, one should choose a relatively low p_T cut to keep more events.

Besides the p_T distributions, there are other optimal observables to distinguish the DPS channel form the SPS channel. The main idea is to make use of the fact that the DPS channel contains two (nearly) independent hard scatterings. For example, the W-boson and dijet production in the $W \otimes jj$ DPS signal are independent, therefore, the dijet system exhibits a null transverse momentum at the leading order and develops a small transverse momentum after including the soft gluon resummation effects [66,67]. The dijet system in the SPS has a large transverse momentum in order to balance the W-boson. The distinct difference in the p_T distribution of the dijet system yields the following optimal observable [9],

$$\Delta^{\text{rel}} p_T = \frac{|p_T(j_1, j_2)|}{|p_T(j_1)| + |p_T(j_2)|}, \qquad (20)$$

where $p_T(j_1, j_2)$ is the vector sum of $p_T(j_1)$ and $p_T(j_2)$. The observable denotes the relative p_T-balance of two tagged jets and tends to be ~ 0 for the DPS events. At the parton level, the $\Delta^{\text{rel}} p_T$ distribution should exhibit a sharp peak at $\Delta^{\text{rel}} p_T = 0$. After parton shower and detector simulations, the sharp peak is smeared and shifted to $\Delta^{\text{rel}} p_T \sim 0.1$ due to soft/collinear radiation and acceptance cuts; see Fig. 8. The $\Delta^{\text{rel}} p_T$ distributions of both the DPS (black curve) and SPS (blue curve) channels have
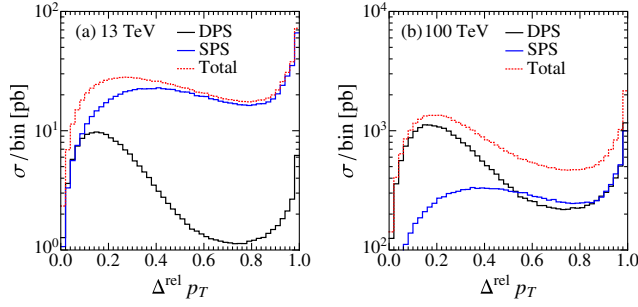
FIG. 8. $\Delta^{\mathrm{rel}} p_T$ distribution for the $W \otimes jj$ channel at the 13 TeV LHC (a) and at the 100 TeV SppC/FCC-hh (b).

FIG. 9. S_ϕ distribution for the $W \otimes jj$ channel at the 13 TeV LHC (a) and at the 100 TeV SppC/FCC-hh (b).

enhancements around $\Delta^{\mathrm{rel}} p_T \sim 1$. It can be understood as follows. One factor is the collinear enhancement of QCD jets, i.e. two colored partons splitting from the same mother parton tend to have similar momentum and enhance $\Delta^{\mathrm{rel}} p_T \sim 1$. Another contribution arises from the so-called Jacobian enhancement. We define the ratio of the p_T magnitude of the two jets as

$$\lambda \equiv \frac{|p_T(j_2)|}{|p_T(j_1)|}, \qquad (21)$$

and obtain

$$\Delta^{\mathrm{rel}} p_T = \frac{\sqrt{1 + \lambda^2 + 2\lambda \cos \Delta\phi_{jj}}}{1 + \lambda}, \qquad (22)$$

where $\Delta\phi_{jj}$ is the azimuthal angle distance of the two jets. A simple algebra yields

$$\begin{aligned} \frac{d\sigma}{d\Delta^{\mathrm{rel}} p_T} &= \frac{d\sigma}{d\Delta\phi_{jj}} \frac{d\Delta\phi_{jj}}{d\Delta^{\mathrm{rel}} p_T} \\ &= \frac{d\sigma}{d\Delta\phi_{jj}} \frac{2\Delta^{\mathrm{rel}} p_T}{\sqrt{[(\Delta^{\mathrm{rel}} p_T)^2 - (\frac{1-\lambda}{1+\lambda})^2][1 - (\Delta^{\mathrm{rel}} p_T)^2]}}. \end{aligned}$$
$$(23)$$

The enhancement around $\Delta^{\mathrm{rel}} p_T \sim 1$ stems from the Jacobian factor. The DPS channel is much less than the SPS channel at the 13 TeV LHC while at the 100 TeV hadron collider the DPS channel dominates.

Another optimal observable is the azimuthal angle correlation between the W system $(\ell^\pm, \not{E}_T)$ and the dijet system (j_1, j_2), defined as

$$S_\phi = \frac{1}{\sqrt{2}} \sqrt{\Delta\phi(\ell^\pm, \not{E}_T)^2 + \Delta\phi(j_1, j_2)^2}, \qquad (24)$$

where $\not{E}_T$ denotes the missing transverse momentum generated by the invisible neutrinos from the W-boson decay. As $(\ell^\pm, \not{E}_T)$ and (j_1, j_2) are produced by two
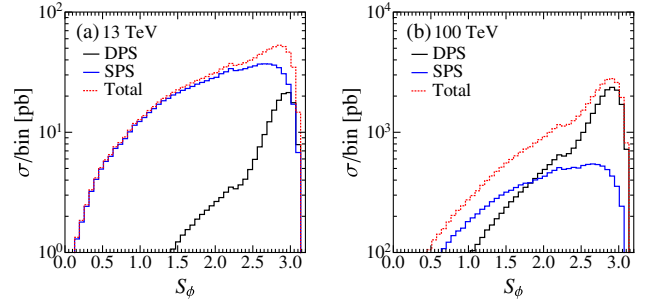
independent scatterings in the DPS channel, S_ϕ tends to be π. In fact, at parton level a sharp peak at $S_\phi = \pi$ will be observed, while the peak is smeared at the hadron level and the peak position is shifted to $S_\phi \sim 2.9$. See the black curves in Fig. 9. On the other hand, for the SPS channel, the final state particles are generally correlated and have a broader distribution; see the blue curves in Fig. 9. The difference in the S_ϕ distributions can be used to identify the DPS events.

B. Collider simulation

We are ready to investigate the potential of detecting the $W \otimes jj$ DPS channel in hadron collisions. The event topology of interest to us is one charged lepton, two hard jets and large $\not{E}_T$. The major SM backgrounds are listed as follows: (i) the irreducible Wjj background with a subsequent decay of $W^\pm \to \ell^\pm \nu$, (ii) the $Z/\gamma^* jj$ background with $Z/\gamma^* \to \ell^+ \ell^-$, (iii) the $t\bar{t}$ pair production with the top quarks decaying semileptonically or purely leptonically, and (iv) the single top production (including t-channel, s-channel, and tW-channel) with the top quark decaying leptonically. In the tW background, we also consider the possibility of the associated W boson decaying into a pair of leptons. The multijet background is shown to be less than 0.5% at the 7 TeV LHC [9] and is ignored in our study. The signal and backgrounds are generated and simulated using the programs mention above. For such weak gauge boson production process, the pileup effect is expected to be small, and indeed, it has been shown to be negligible at the 7 TeV LHC for the DPS $W \otimes jj$ searches [9]. We ignore the pile-up contamination in our simulation hereafter. Following [9,62], we impose four *basic* kinematics cuts in sequence:

(1) exactly one charged lepton with $p_T^\ell \geq 35$ GeV, $|\eta^\ell| \leq 2.5$ at the 13 TeV LHC and $|\eta^\ell| \leq 4$ at the 100 TeV SppC/FCC-hh;
(2) exactly two hard jets with $p_T^j \geq 25$ GeV and $|\eta^j| \leq 2.5$ at the 13 TeV LHC while $p_T^j \geq 50$ GeV and $|\eta^j| \leq 5$ at the 100 TeV SppC/FCC-hh;
(3) $\not{E}_T \geq 30$ GeV;
(4) $M_T > 50$ GeV.

TABLE III. Cross sections (in the unit of picobarn) of the DPS $W \otimes jj$ process and the SM backgrounds at the 13 TeV LHC (top) and at the 100 TeV SppC/FCC-hh (bottom). We choose $\sigma_{\text{eff}} = 15$ mb and impose he kinematic cuts listed in each column sequentially.

13 TeV	Gen.	Cut-1	Cut-2	Cut-3	Cut-4
DPS $W(\to l\nu_l)jj$	1138.94	248.76	53.85	36.35	35.07
$W(\to l\nu_l)jj$	18 591.50	3406.39	381.77	223.44	184.72
$t\bar{t}$ (all decay modes)	461.00	76.16	10.26	8.46	6.61
$t(\to bl\nu_l)j$	36.58	13.44	5.78	4.09	3.36
tW (all decay modes)	39.45	7.21	2.01	1.50	1.15
$Z(\to ll)jj$	1904.81	513.83	83.60	8.31	4.72
100 TeV					
DPS $W(\to l\nu_l)jj$	128 283	32 860.7	1841.97	1259.76	1047.49
$W(\to l\nu_l)jj$	189 865	38 856.1	2755.1	1869.18	1393.42
$t\bar{t}$ (all decay modes)	30 675.9	5085.14	1248.42	1018.41	749.72
$t(\to bl\nu_l)j$	915.11	343.69	111.81	81.42	64.56
tW (all decay modes)	1934.79	364.42	114.52	89.82	63.21
$Z(\to ll)jj$	14 044.1	4756.51	552.36	117.81	69.98

Here, M_T denotes the transverse mass of the ($\ell^{\pm}$, $\not{E}_T$) system, defined as

$$M_T \equiv \sqrt{2 \cdot p_T^{\ell} \cdot \not{E}_T \cdot (1 - \cos\Delta\phi)}, \qquad (25)$$

where ϕ denotes the open angle between the charged lepton and missing momentum in the transverse plane.

Among the four cuts listed above, the first cut (cut-1), the second cut (cut-2) and the third cut (cut-3) are meant to trigger the event. At the 100 TeV SppC/FCC-hh, we impose a harder cut on the jet p_T to suppress the QCD backgrounds. We also extend the lepton coverage to collect more signals. We adopt the same lepton p_T cut and $\not{E}_T$ cut at the 13 TeV and 100 TeV hadron colliders as both the lepton p_T and $\not{E}_T$ distributions of the DPS signal events have a unchanged Jacobian peak around $m_W/2$.

In the simulation, we choose σ_{eff} as the average value of current experimental results $\sigma_{\text{eff}} = 15$ mb. When generating both the signal and background events in MadGraph, we impose loose cuts on jets at the parton level as follows:

$$p_T^j \geq 10 \text{ GeV}, \qquad |\eta^j| < 5. \qquad (26)$$

We then use Pythia for parton shower and jet merging. The cross section (in the unit of picobarn) of the signal and background processes after Pythia (denoted as "Gen.") are summarized in the second column of Table III. Next, we adapt the Delphes for particle identification and then impose the four basic cuts. The last four columns in Table III show the cross section after imposing the four selection cuts sequentially. The SPS Wjj channel is the dominant background at the 13 and 100 TeV colliders. It is about 5 times larger than the DPS signal at the 13 TeV LHC. The subleading background is from top quark pair production which is not important at the 13 TeV LHC. At the 100 TeV

collider, owing to the dramatically enhanced productions of the dijet subprocess, the cross section of the DPS signal is comparable to the SPS Wjj background. For the same reason, the top-quark pair background becomes important.

As a matter of fact, the four kinematics cuts only select events that from Wjj final state, but do not care about whether they are from DPS or SPS. So it is necessary to introduce the observables discussed last subsection to suppress SPS events and manifest DPS ones. A variable f^{DPS} is defined to quantitatively describe the fraction of the DPS signal event in the total event collected. It is defined as [10]

$$f^{\text{DPS}} = \frac{\sigma_{\text{DPS}}}{\sigma^{\text{DPS}} + \sum_i \sigma_{\text{Background}}^i}, \qquad (27)$$

where summing over all the SM backgrounds are understood. As shown in Table IV, $f^{\text{DPS}} = 15\%$ after imposing the four basic cuts at the 13 TeV LHC. The fraction

TABLE IV. Cross sections (in the unit of picobarn) of the DPS signal and backgrounds after imposing optimal cuts at the 13 TeV LHC (top) and at the 100 TeV SppC/FCC-hh (bottom). We choose $\sigma_{\text{eff}} = 15$ mb.

13 TeV	DPS Wjj	Wjj	$t\bar{t}$	tj	tW	Zjj	f^{DPS}
Basic cuts	35.07	184.72	6.61	3.36	1.15	4.72	0.15
$S_\phi > 2.5$	23.91	57.16	1.57	0.77	0.22	1.66	0.28
Or							
$\Delta^{\text{rel}} p_T < 0.2$	12.73	23.06	0.56	0.37	0.08	0.65	0.34
100 TeV							
Basic cuts	1047.49	1393.42	749.72	64.56	63.21	69.98	0.31
$S_\phi > 2.5$	479.09	417.96	173.23	19.99	11.36	28.68	0.42
Or							
$\Delta^{\text{rel}} p_T < 0.2$	312.43	263.56	92.63	12.84	6.18	14.33	0.45

increases dramatically to $f^{\mathrm{DPS}} = 31\%$ at the 100 TeV collider.

We can make use of the $\Delta^{\mathrm{rel}} p_T$ and S_ϕ distributions to improve f^{DPS}. In this study, we impose a cut on either $\Delta^{\mathrm{rel}} p_T$ or S_ϕ and do not require cuts on both, because cutting on one variables is good enough for identifying the DPS events. We demand either

$$\Delta^{\mathrm{rel}} p_T \leq 0.2, \tag{28}$$

or

$$S_\phi > 2.5. \tag{29}$$

The cross sections of the DPS signal and backgrounds after the optimal cut are presented in Table IV; see the third row for the 13 TeV LHC and the sixth row for a 100 TeV collider. It shows that either of the optimal cuts can efficiently suppress the SM backgrounds and increase the fraction f^{DPS} dramatically. We notice that the $\Delta^{\mathrm{rel}} p_T$ cut is slightly better than the S_ϕ cut. It yields $f^{\mathrm{DPS}} \sim 30\%$ at the 13 TeV LHC and $f^{\mathrm{DPS}} \sim 45\%$ at the 100 TeV colliders.

The numerical results of the DPS signal channel listed in Tables III and IV are calculated with $\sigma_{\mathrm{eff}} = 15$ mb. Below, we study how well one can measure σ_{eff} from various distributions.

C. Determining σ_{eff}

There are two methods to measure σ_{eff}. One way is to extract σ_{eff} directly from the number of events collected experimentally. From the master formula given in Eq. (1), one can derive σ_{eff} as follows,

$$\sigma_{\mathrm{eff}} = \frac{\sigma_W^{\mathrm{SPS}} \times \sigma_{jj}^{\mathrm{SPS}} \times \epsilon \times \mathcal{L}}{N_{\mathrm{DPS}}}$$
$$= \frac{\sigma_W^{\mathrm{SPS}} \times \sigma_{jj}^{\mathrm{SPS}} \times \epsilon \times \mathcal{L}}{N_{\mathrm{OBS}} - N_{\mathrm{BKGD}}}, \tag{30}$$

where N_{DPS} denotes the number of DPS signal events, N_{BKGD} labels the number of events of the backgrounds predicted by the Monte Carlo simulation, and N_{OBS} denotes the total number of events which includes both signal and backgrounds events, i.e.

$$N_{\mathrm{OBS}} = N_{\mathrm{DPS}} + N_{\mathrm{BKGD}}. \tag{31}$$

$\mathcal{L}$ is the integrated luminosity, and ϵ represents the cut efficiency derived from theoretical simulation. In this study, we adopt the four basic cuts plus one optimal cut $\Delta^{\mathrm{rel}} p_T < 0.2$ to maximize the fraction f^{DPS}. The cut efficiencies of the signal and background processes are derived from those numbers shown in Table IV.

The uncertainty of measuring σ_{eff} arises from both statistical and systematics errors. In this study, the statistic

error is assumed to obey a Gaussian distribution, i.e. $\delta N_{\mathrm{stat}} = \sqrt{N_{\mathrm{OBS}}}$. The systematic error can be known only after real experiments, and for a conservative estimation, we choose two benchmark uncertainties, $f_{\mathrm{syst}} = 15\%$ and 25%, throughout this study. The total uncertainty of N_{OBS} is given by

$$\delta N = \sqrt{(\delta N_{\mathrm{stat}})^2 + (\delta N_{\mathrm{syst}})^2}, \tag{32}$$

with

$$\delta N_{\mathrm{stat}} = \sqrt{N_{\mathrm{OBS}}}, \qquad \delta N_{\mathrm{syst}} = f_{\mathrm{syst}} \times N_{\mathrm{OBS}}. \tag{33}$$

The accuracy of measuring σ_{eff} can be determined from Eq. (30) for a given σ_{eff} input. Figure 10 displays the extracted σ_{eff} as a function of the input σ_{eff} at the 13 TeV LHC (a) and 100 TeV SppC/FCC-hh (b) with an integrated luminosity of 300 fb^{-1}. The blue bands denote the accuracy of σ_{eff} measurement with the choice of systematic uncertainty $f_{\mathrm{syst}} = 15\%$ while the green bands label the case of $f_{\mathrm{syst}} = 25\%$. Since the DPS rate is very large after imposing the basic and optimal cuts, the statistical uncertainty is well under control and the systematic uncertainty plays the leading role. Therefore, the uncertainty bands shown in Fig. 10 remain almost the same in the case of high luminosities.

It is obvious that the event counting method is not good for measuring σ_{eff}. A better method to improve the accuracy of σ_{eff} measurement is to fit the $\Delta^{\mathrm{rel}} p_T$ and S_ϕ distributions [8–10]. In the study, we first generate the DPS events for a given σ_{eff} input and then combine the DPS events with the SPS backgrounds to get the pseudoexperiment data. Each bin of the distributions are allowed to exhibit a fluctuation of $\pm \delta N_i$ defined below. After that, we rescale the DPS events as a function of σ_{eff} to fit the pseudodata to obtain the accuracy of the σ_{eff} measurement. In the fitting, we define the χ^2 function as
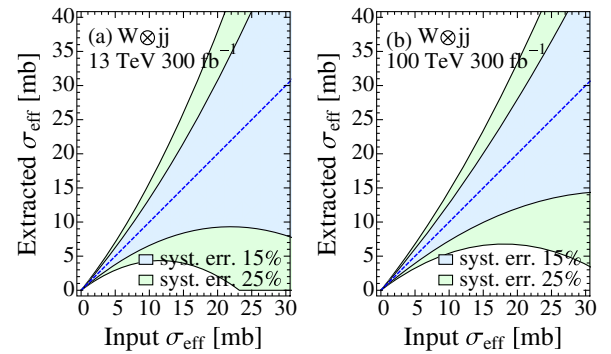

FIG. 10. The projected accuracy of measuring σ_{eff} directly from event-number counting at the 13 TeV LHC (a) and 100 TeV SppC/FCC-hh (b).

$$\chi^2 = \sum_{i=1}^{N} \frac{(N_i^{\text{th}} - N_i^{\text{exp}})^2}{(\delta N_i)^2}, \qquad (34)$$

where N_i^{exp} and δN_i denote the number of events and uncertainty in the ith bin of the psesudodata distribution, respectively, and N_i^{th} denotes the number of events in the ith bin of the rescaled DPS distribution. The δN_i contains both statistical and systematic uncertainties, defined similarly to Eq. (33) as

$$\delta N_i = \sqrt{N_i + f_{\text{syst}}^2 N_i^2}. \qquad (35)$$

In the $W \otimes jj$ channel, we divide the $\Delta^{\text{rel}} p_T$ and S_ϕ distributions into 50 bins, i.e. $N = 50$. From the χ^2 analysis we obtain the accuracy of σ_{eff} measurement at the 1σ confidence level for the two benchmark systematic uncertainties.

We examine both the $\Delta^{\text{rel}} p_T$ and S_ϕ distributions at the 13 TeV LHC and 100 TeV colliders with an integrated luminosity of 300 fb^{-1}. Figure 11 shows the expected σ_{eff}'s versus the input values. The input values of σ_{eff} are chosen to be 10 mb, 15 mb and 20 mb. The red-circle symbol denotes the $\sigma_{\text{eff}}^{\text{fit}}$ obtained in fitting the $\Delta^{\text{rel}} p_T$ distribution while the red-triangle symbol labels the one obtained from the S_ϕ distribution. It turns out that one can get a better measurement of σ_{eff} in the $\Delta^{\text{rel}} p_T$ distribution.

The $\sigma_{\text{eff}}^{\text{fit}}$'s obtained from the $\Delta^{\text{rel}} p_T$ distribution are listed as follows:

(i) $\sigma_{\text{eff}}^{\text{in}} = 10$ mb

$$\sigma_{\text{eff}}^{\text{fit}} = 10^{+0.91(+9.1\%)}_{-0.77(-7.7\%)}, \quad 10^{+1.62(+16.2\%)}_{-1.22(-12.2\%)}, \quad 13\,\text{TeV},$$

$$\sigma_{\text{eff}}^{\text{fit}} = 10^{+0.55(+5.5\%)}_{-0.50(-5.5\%)}, \quad 10^{+0.95(+9.5\%)}_{-0.80(-8.0\%)}, \quad 100\,\text{TeV};$$
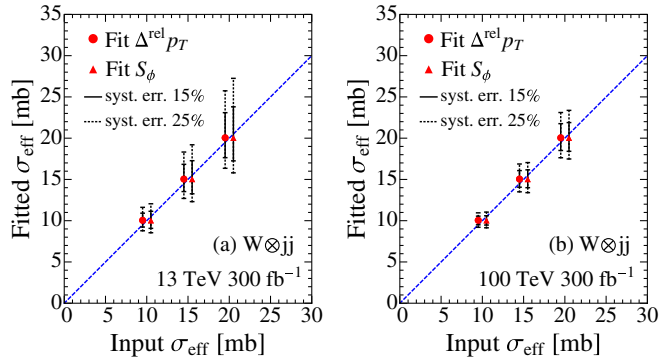

FIG. 11.   The fitted σ_{eff} as a function of the σ_{eff} input obtained in the $W \otimes jj$ channel at the 13 TeV LHC (a) and 100 TeV colliders (b) with an integrated luminosity of 300 fb^{-1}.

(ii) $\sigma_{\text{eff}}^{\text{in}} = 15$ mb

$$\sigma_{\text{eff}}^{\text{fit}} = 15^{+1.83(+12.2\%)}_{-1.47(-9.8\%)}, \quad 15^{+3.32(+22.1\%)}_{-2.30(-15.3\%)} \quad 13\,\text{TeV},$$

$$\sigma_{\text{eff}}^{\text{fit}} = 15^{+1.07(+7.1\%)}_{-0.94(-6.3\%)}, \quad 15^{+1.87(+12.5\%)}_{-1.50(-10.0\%)}, \quad 100\,\text{TeV};$$

(iii) $\sigma_{\text{eff}}^{\text{in}} = 20$ mb

$$\sigma_{\text{eff}}^{\text{fit}} = 20^{+3.09(+15.5\%)}_{-2.36(-11.8\%)}, \quad 20^{+5.74(+28.7\%)}_{-3.65(-18.3\%)}, \quad 13\,\text{TeV},$$

$$\sigma_{\text{eff}}^{\text{fit}} = 20^{+1.76(+8.8\%)}_{-1.49(-7.5\%)}, \quad 20^{+3.11(+15.6\%)}_{-2.37(-11.9\%)}, \quad 100\,\text{TeV},$$

where the first value of $\sigma_{\text{eff}}^{\text{fit}}$ is for $f_{\text{syst}} = 15\%$ while the second value for $f_{\text{syst}} = 25\%$. The superscript and subscript denotes the upper and lower error at the 1σ confidential level, respectively. The percentage shown in the super-scripts and subscripts denotes the percentage of the error relative to the mean fitting value of $\sigma_{\text{eff}}^{\text{fit}}$. The asymmetric errors is owing to the inverse relation between N_i^{th} and σ_{eff}. If we fit $1/\sigma_{\text{eff}}$ rather than σ_{eff}, then we end up with symmetric errors.

We emphasize that, owing to the fact that the systematic errors dominate over the statistical errors, increasing luminosity does not significantly improve the accuracy of σ_{eff} measurement. Of course, accumulating more data helps with reducing the systematic errors, but on the assumption of fixed systematic uncertainty, those uncertainties of $\sigma_{\text{eff}}^{\text{fit}}$ shown in Fig. 11 remain almost the same for a higher luminosity. On the other hand, increasing colliding energy will greatly reduce the uncertainties of σ_{eff} measurements. The rate of the DPS channel increases dramatically with colliding energy such that the DPS channel dominates over the SM background. That enables us to reach a better precision of $\sigma_{\text{eff}}^{\text{fit}}$.

Two methods of measuring σ_{eff} are presented above; one is based on event counting, the other is based on fitting the characteristic kinematics distributions of the DPS optimal observables. The fitting method works much better than the event counting method in measuring σ_{eff}. Therefore, we adopt the fitting method hereafter.

V. THE $Z \otimes jj$ CHANNEL

Now consider another interesting DPS channel, the $Z \otimes jj$ process. The channel also has advantages of clear event triggering and large production rate. A parton level analysis of the MPI contribution to the $Z \otimes$ jets final states has been carried out in Ref. [48] in which three colliding energies (8, 10 and 14 TeV) are studied. A dynamical approach to such final state within the Pythia event generator is studied in Ref. [53]. In this work, we present a hadron level study in hadron collisions.
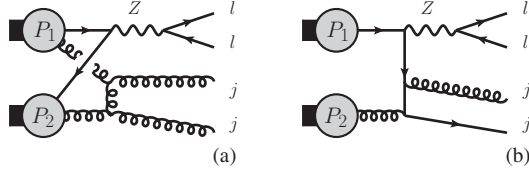
FIG. 12. Representative Feynman diagrams of the $Z \otimes jj$ DPS channel (a) and the Zjj SPS background (b).

A. Kinematics distributions

The pictorial illustration of the $Z \otimes jj$ channel and the SPS Zjj background are plotted Fig. 12. The $Z \otimes jj$ events are combined from two sets of hadron level event files of the SPS subprocess $Z(\to \ell^+\ell^-)$ (merged with Zj) and the jj production (merged with jjj). Similar to the $W \otimes jj$ channel, the feature of two independent subprocesses gives rise to characteristic kinematics distributions which can be used to distinguish between the DPS signal and the backgrounds.

Figure 13 displays the transverse momentum distributions of the leading-p_T jet (a, b) and of the leading-p_T charged leptons (c, d) at the 13 TeV LHC and the 100 TeV colliders, after Delphes reconstruction. Similar to the case of $W \otimes jj$ channel, the charged lepton p_T distribution of the $Z \otimes jj$ events exhibits a Jacobi peak at $\sim m_Z/2$ while the distribution of the Zjj SPS events tends to have a long tail towards the large p_T region. The jet p_T distribution of the $Z \otimes jj$ events peaks around the Delphes reconstruction threshold $p_T = 20$ GeV and drops rapidly. On the other hand, in order to balance the on-shell Z boson, the p_T distribution of the leading jets in the Zjj SPS events has a long tail in large p_T region. Thus, we can impose a hard p_T cut on the jet and a loose cut on the charged lepton to retain more DPS events.

Consider the optimal distributions to discriminate the DPS signal from the SPS backgrounds. Following the study of the $W \otimes jj$ channel, we define a relative p_T balance of two jets as

$$\Delta_j^{\mathrm{rel}} p_T = \frac{|p_T(j_1, j_2)|}{|p_T(j_1)| + |p_T(j_2)|}. \qquad (36)$$

Figures 14(a) and 14(b) display the $\Delta_j^{\mathrm{rel}} p_T$ distributions of the DPS signal (black curve) and the Zjj background (blue). Note that the $\Delta_j^{\mathrm{rel}} p_T$ distributions of the $Z \otimes jj$ channel are quite alike in shape to those distributions of the $W \otimes jj$ channel. It is no surprise as the kinematics of the two jets is identical in the both DPS channels. The peaks around $\Delta_j^{\mathrm{rel}} p_T \sim 1$ are due to the Jacobian factor explained in Eq. (23).

One advantage of the $Z \otimes jj$ channel is that one has full information of the two charged leptons from the Z boson decay. That enables us to define a relative p_T balance of two charged leptons as following:
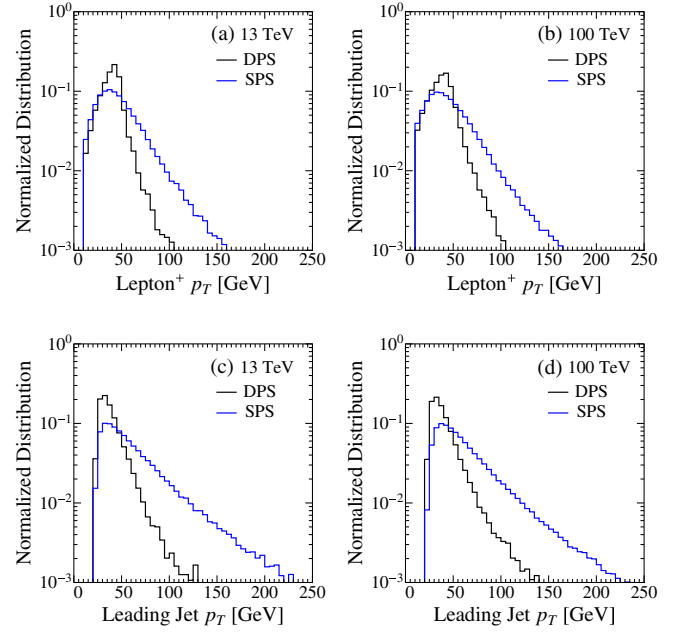

FIG. 13. The p_T distributions of the leading jet (a, b) and of the leading charged leptons (c, d) for the $Z \otimes jj$ channel at the 13 TeV LHC and the 100 TeV SppC/FCC-hh.

$$\Delta_\ell^{\mathrm{rel}} p_T = \frac{|p_T(\ell^+, \ell^-)|}{|p_T(\ell^+)| + |p_T(\ell^-)|} \approx \frac{|p_T(Z)|}{|p_T(\ell^+)| + |p_T(\ell^-)|}, \qquad (37)$$

and plot the $\Delta_\ell^{\mathrm{rel}} p_T$ distributions in Figs. 14(c) and 14(d). In both the signal and background channels, most charged
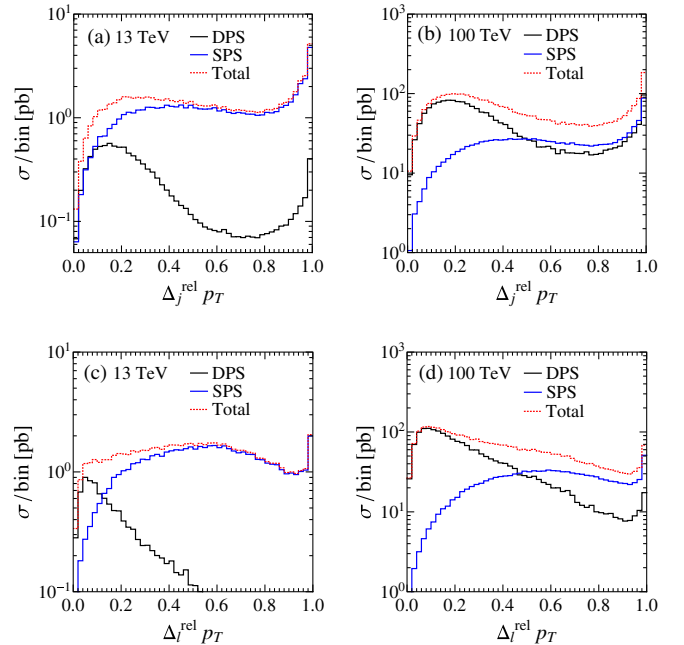

FIG. 14. $\Delta_j^{\mathrm{rel}} p_T$ and $\Delta_\ell^{\mathrm{rel}} p_T$ distributions for the $Z \otimes jj$ channel at the 13 TeV (a, c) and 100 TeV colliders (b, d).

leptons are populated in the region of $p_T \sim m_Z/2$ such that the value of the denominator of $\Delta_\ell^{\mathrm{rel}} p_T$ is around 90 GeV. For the DPS signal, $p_T(Z) \sim 0$, thus rendering the $\Delta_\ell^{\mathrm{rel}} p_T$ distribution peaking around 0; see the black curves. For the Zjj SPS background, the Z boson, as balanced by the two hard jets, tends to have a hard p_T. That renders the $\Delta_\ell^{\mathrm{rel}} p_T$ distributions of the Zjj background peak around $0.4 \sim 0.6$.

The third optimal observable is the azimuthal angle correlation of the Z system and jj system, defined as

$$S_\phi \equiv \frac{1}{\sqrt{2}} \sqrt{\Delta\phi(\ell^+, \ell^-)^2 + \Delta\phi(j_1, j_2)^2}. \quad (38)$$

We plot the S_ϕ distributions in Fig. 15 at the 13 TeV (a) and 100 TeV colliders (b). For the DPS channel, the two jets fly away almost back-to-back, i.e. $\Delta\phi(j_1, j_2) \sim \pi$. Similarly, $\Delta\phi(\ell^+, \ell^-) \sim \pi$. Therefore, the S_ϕ distribution of the DPS signal peaks around 3; see the black curves. On the other hand, the two jets in the background events tend to move parallel such that $\Delta\phi(j_1, j_2) \sim 0$. That yields $S_\phi \sim 2.1$–2.5 in the background; see the blue curves.

B. Collider simulation

The event topology of the $Z \otimes jj$ signal is two charged leptons with opposite charges and two hard jets. The main SPS backgrounds are listed as follows: (i) the irreducible Zjj background with $Z \rightarrow \ell^+\ell^-$; (ii) the WZ pair production with $W \rightarrow q\bar{q}'$ and $Z \rightarrow \ell^+\ell^-$; (iii) the $t\bar{t}$ pair production with the top-quark pair decaying either semi-leptonically or leptonically; (iv) the tW single-top production with $t \rightarrow b\ell^\pm\nu$ and $W^\pm \rightarrow \ell^\pm\nu$. Following Refs. [62,68], we impose four basic kinematics cuts in sequence:

(1) exactly two opposite charged leptons with $p_T^\ell \geq 25$ GeV, $|\eta^\ell| \leq 2.5$ at the 13 TeV LHC and $|\eta^\ell| \leq 4$ at the 100 TeV SppC/FCC-hh;

(2) exactly two hard jets with $p_T^j \geq 30$ GeV and $|\eta^j| \leq 2.5$ at the 13 TeV LHC while $p_T^j \geq 50$ GeV and $|\eta^j| \leq 5$ at the 100 TeV SppC/FCC-hh;

(3) $\not{E}_T \leq 30$ GeV;
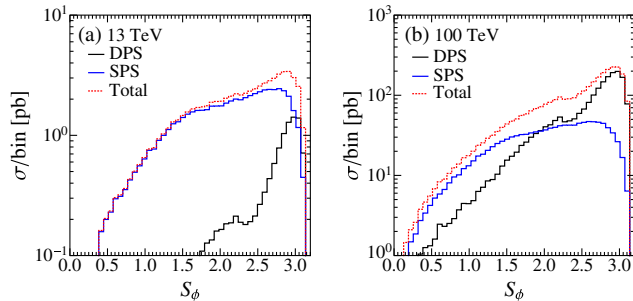
(4) $M_{\ell\ell} \in [71, 111]$ GeV.

FIG. 15. S_ϕ distribution for the $Z \otimes jj$ channel at the 13 TeV LHC (a) and 100 TeV colliders (b).

Similar to the case of $W \otimes jj$ channel, we enlarge the jet p_T^j cut and the lepton $|\eta^\ell|$ cut to cover more events at the 100 TeV colliders. The third cut aims at reducing the backgrounds involving W bosons, e.g. the $t\bar{t}$ and tW backgrounds. The fourth cut requires that the invariant mass of the two charged leptons lies within the mass window of Z boson.

We choose the input value of $\sigma_{\mathrm{eff}} = 15$ mb in our simulation. After generating both the signal and background events in MadGraph with $p_T^j \geq 10$ GeV and $|\eta^j| < 5$, we pass them to Pythia for parton shower and merging. The cross section (in the unit of picobarn) of the signal and background processes after Pythia (denoted as "Gen.") are summarized in the second column of Table V. Next, we use Delphes for particle identifications and then impose the four kinematics cuts. The last four columns in Table V show the cross section after imposing the four selection cuts sequentially.

After the fourth cut, the intrinsic Zjj SPS background still dominates over the $Z \otimes jj$ DPS signal at the 13 TeV LHC, say $\sigma(Zjj) \sim 7 \times \sigma(Z \otimes jj)$. Thanks to large colliding energy of the 100 TeV colliders, the $Z \otimes jj$ DPS signal and the intrinsic Zjj background are comparable. Other reducible backgrounds turn out to be negligible.

We make use of the characteristic distributions of $\Delta_\ell^{\mathrm{rel}} p_T$, $\Delta_j^{\mathrm{rel}} p_T$ and S_ϕ to further suppress the intrinsic Zjj background. In this study, we demand one and only one cut in the following list:

$$\Delta_\ell^{\mathrm{rel}} p_T \leq 0.2,$$
$$\Delta_j^{\mathrm{rel}} p_T \leq 0.2,$$
$$S_\phi > 2.5. \quad (39)$$

TABLE V. Cross sections (in the unit of picobarn) of the DPS $Z \otimes jj$ process and the SM backgrounds at the 13 TeV LHC (top) and at the 100 TeV SppC/FCC-hh (bottom). We choose $\sigma_{\mathrm{eff}} = 15$ mb and impose the kinematic cuts listed in each column sequentially.

13 TeV	Gen.	Cut-1	Cut-2	Cut-3	Cut-4
DPS $Z(\rightarrow\ell^+\ell^-)jj$	108.92	28.10	3.60	3.46	3.40
$Z(\rightarrow\ell^+\ell^-)jj$	1904.81	336.35	24.41	22.74	22.29
$W(\rightarrow jj)Z(\rightarrow\ell^+\ell^-)$	1.623	0.45	0.14	0.13	0.12
$t\bar{t}$ (all decay modes)	461.00	6.52	2.64	0.40	0.12
tW (all decay modes)	39.45	0.68	0.16	0.03	0.01

100 TeV					
DPS $Z(\rightarrow\ell^+\ell^-)jj$	13 376.2	3974.08	175.71	139.70	137.21
$Z(\rightarrow\ell^+\ell^-)jj$	14 044.1	2673.22	240.68	194.4	190.34
$W(\rightarrow jj)Z(\rightarrow\ell^+\ell^-)$	24.35	6.91	1.70	1.30	1.27
$t\bar{t}$ (all decay modes)	30 675.9	416.44	132.66	17.63	4.17
tW (all decay modes)	1934.79	33.76	6.53	0.79	0.13

TABLE VI. Cross sections (in the unit of picobarn) of the DPS signal and backgrounds after imposing optimal cuts at the 13 TeV LHC (top) and at the 100 TeV SppC/FCC-hh (bottom). We choose $\sigma_{\rm eff} = 15$ mb.

13 TeV	DPS Zjj	Zjj	WZ	$t\bar{t}$	tW	$f^{\rm DPS}$
Basic cuts	3.40	22.29	0.12	0.12	0.01	0.13
$S_\phi > 2.5$	2.21	7.47	0.03	0.04	0.00	0.23
Or $\Delta_\ell^{\rm rel} p_T < 0.2$	1.60	1.90	0.01	0.01	0.00	0.45
Or $\Delta_j^{\rm rel} p_T < 0.2$	1.23	2.77	0.01	0.02	0.00	0.31

100 TeV						
Basic cuts	137.21	190.34	1.27	4.17	0.13	0.41
$S_\phi > 2.5$	73.19	62.35	0.27	1.38	0.03	0.53
Or $\Delta_\ell^{\rm rel} p_T < 0.2$	38.68	10.43	0.05	0.27	0.00	0.78
Or $\Delta_j^{\rm rel} p_T < 0.2$	46.13	35.05	0.17	0.84	0.01	0.56

We do not require all of the three cuts simply because cutting on one variable is good enough to enhance the DPS signal. The cross sections of the DPS signal and backgrounds after the optimal cut are presented in Table VI. See the third row for cross sections at the 13 TeV LHC and the sixth row for cross sections at the 100 TeV colliders. It shows that the optimal cut efficiently suppress the SM backgrounds and increase $f^{\rm DPS}$. We also notice that the $\Delta_\ell^{\rm rel} p_T$ cut is much better than the other two cuts. It yields $f^{\rm DPS} \sim 45\%$ at the 13 TeV LHC and $f^{\rm DPS} \sim 80\%$ at the 100 TeV colliders. It is very promising to observe the DPS signal at the LHC and future hadron colliders.

C. Measuring $\sigma_{\rm eff}$

We fit the distributions of $\Delta_\ell^{\rm rel} p_T$, $\Delta_j^{\rm rel} p_T$ and S_ϕ to measure $\sigma_{\rm eff}$. Again, we choose three benchmark inputs ($\sigma_{\rm eff}^{\rm input} = 10, 15, 20$ mb) and assume the systematic uncertainties to be 15% and 25% in the fitting analysis.

Figure 16 shows the fitted $\sigma_{\rm eff}^{\rm fit}$ as a function of the input $\sigma_{\rm eff}^{\rm input}$ at the 13 TeV LHC (a) and 100 TeV (b) colliders with an integrated luminosity of 300 fb^{-1}. The circle (triangle,
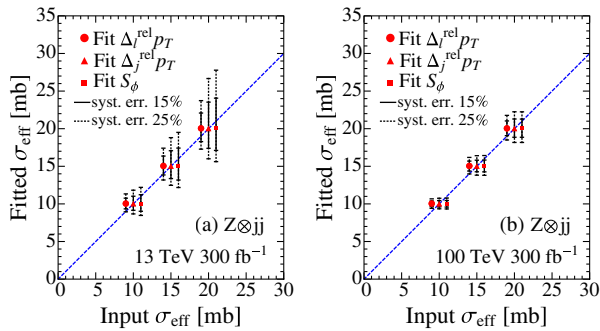

FIG. 16. The fitted $\sigma_{\rm eff}$ as a function of the $\sigma_{\rm eff}$ input obtained in the $Z \otimes jj$ channel at the 13 TeV LHC (a) and 100 TeV colliders (b) with an integrated luminosity of 300 fb^{-1}.

box) symbol denotes $\sigma_{\rm eff}^{\rm fit}$ obtained from fitting the $\Delta_\ell^{\rm rel} p_T$ ($\Delta_j^{\rm rel} p_T$, S_ϕ) distribution, respectively. Fitting the $\Delta_\ell^{\rm rel} p_T$ distribution gives rise to the best accuracy of $\sigma_{\rm eff}^{\rm fit}$, which are listed as follows:

(i) $\sigma_{\rm eff}^{\rm in} = 10$ mb

$$\sigma_{\rm eff}^{\rm fit} = 10_{-0.66(-6.6\%)}^{+0.76(+7.6\%)}, \quad 10_{-1.05(-10.5\%)}^{+1.33(+13.3\%)}, \quad 13\,{\rm TeV},$$

$$\sigma_{\rm eff}^{\rm fit} = 10_{-0.37(-3.7\%)}^{+0.39(+3.9\%)}, \quad 10_{-0.59(-5.9\%)}^{+0.67(+6.7\%)}, \quad 100\,{\rm TeV};$$

(ii) $\sigma_{\rm eff}^{\rm in} = 15$ mb

$$\sigma_{\rm eff}^{\rm fit} = 15_{-1.15(-7.7\%)}^{+1.36(+9.1\%)}, \quad 15_{-1.82(-12.1\%)}^{+2.41(+16.1\%)} \quad 13\,{\rm TeV},$$

$$\sigma_{\rm eff}^{\rm fit} = 15_{-0.63(-4.2\%)}^{+0.69(+4.6\%)}, \quad 15_{-1.02(-6.8\%)}^{+1.18(+7.9\%)}, \quad 100\,{\rm TeV};$$

(iii) $\sigma_{\rm eff}^{\rm in} = 20$ mb

$$\sigma_{\rm eff}^{\rm fit} = 20_{-1.72(-8.6\%)}^{+2.08(+10.4\%)}, \quad 20_{-2.72(-13.6\%)}^{+3.73(+18.7\%)}, \quad 13\,{\rm TeV},$$

$$\sigma_{\rm eff}^{\rm fit} = 20_{-0.93(-4.7\%)}^{+1.03(+5.2\%)}, \quad 20_{-1.50(-7.5\%)}^{+1.77(+8.9\%)}, \quad 100\,{\rm TeV},$$

where the first value of $\sigma_{\rm eff}^{\rm fit}$ is for $f_{\rm syst} = 15\%$ while the second value for $f_{\rm syst} = 25\%$. The superscript and subscript denotes the upper and lower error and the percentage denotes the fraction of the error normalized to the mean value of $\sigma_{\rm eff}^{\rm fit}$.

The systematic error also dominates over the statistical error in the $Z \otimes jj$ channel; therefore, increasing luminosity cannot significantly improve the accuracy of $\sigma_{\rm eff}^{\rm fit}$. Of course, accumulating more data helps with reducing the systematic errors, but on the assumption of fixed systematic uncertainty as we made, those uncertainties of $\sigma_{\rm eff}^{\rm fit}$ shown in Fig. 16(a) remain almost the same for the case of a high luminosity machine. Increasing collider energy dramatically enhances the production rate of the DPS signal such that the DPS signal dominates over the SM backgrounds after the optimal cut. That greatly improves the fitting accuracy of $\sigma_{\rm eff}^{\rm fit}$, and all the three distributions yields comparable accuracies of $\sigma_{\rm eff}^{\rm fit}$; see Fig. 16(b).

We note that, in comparison with the $W \otimes jj$ channel, one can achieve a better measurement of $\sigma_{\rm eff}$ in the $Z \otimes jj$ channel. To our best knowledge, there is no experimental search for the DPS signal in the $Z \otimes jj$ channel yet. Our study shows that the relative p_T balance of two charged leptons, $\Delta_\ell^{\rm rel} p_T$, is the best variable to do the job.

VI. THE $W^\pm \otimes W^\pm$ CHANNEL

The $W^\pm \otimes W^\pm$ channel has a clean collider signature of two same-sign charged leptons and large missing transverse momentum induced by neutrinos. See Fig. 17 for a pictorial illustration. The channel is often believed to offer a unambiguous measurement of $\sigma_{\rm eff}$ and has been extensively
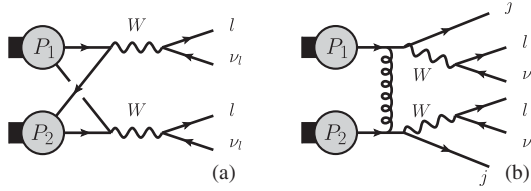
FIG. 17. A pictorial illustration of the $W^\pm \otimes W^\pm$ DPS channel (a) and the $W^\pm W^\pm jj$ SPS background (b).

studied in the literature [11–14,39,56,57,69]. In Ref. [69], a study considering the parton correlations is performed, base on the light-front quark model of Ref. [41]. Below we explore the $W^\pm \otimes W^\pm$ production at the 13 TeV LHC and future 100 TeV colliders within the SF model.

A. Kinematics distributions

The collider signature of the $W^\pm \otimes W^\pm$ DPS channel is two charged leptons plus $\not{E}_T$. As shown in Fig. 17, the $W^\pm W^\pm jj$ SPS background has two additional jets in the final state. It can mimic the DPS signal when the two additional jets either have a small p_T or appear outside of the detector coverage. We veto "hard" jet activities in the central region of the detector in the $W^\pm W^\pm jj$ SPS background; i.e. we reject any hard jet satisfying $p_T > 25$ GeV and $|\eta| < 2.5$ at the 13 TeV while $p_T > 50$ GeV and $|\eta| < 5$ GeV at the 100 TeV colliders. Figure 18 shows the p_T distribution of the leading charged lepton. Owing to the feature of independent subprocesses of the DPS channel, the p_T distribution of the leading charged lepton has a Jacobian peak around $p_T \sim m_W/2$. The subleading lepton also exhibits such a Jacobian peak in its p_T distribution. On the contrary, the charged leptons in the SPS background are populated more around the cut threshold and have a long tail stretching far into the large p_T region.

The drawback of the $W^\pm \otimes W^\pm$ channel is the two invisible neutrinos, which yield a collider signature of missing transverse momentum and cannot be fully reconstructed. It is hard to determine the longitudinal component

of the neutrino momentum at hadron colliders. Such a difficulty has bothered us for a long time in the single W-boson production through the Drell-Yan channel [67] and single-top quark productions [70]. The situation is even worse when the final state consists of two or more invisible neutrinos. Usually, one has to use the on-shell conditions of intermediate state particles to reconstruct the neutrino kinematics [71,72]. However, in the $W^\pm \otimes W^\pm$ channel, we do not have enough information to determine the two neutrinos' momenta, which, unfortunately, are the key to reconstructing two subsystems. Therefore, we cannot examine the independent correlations of two subsystems to probe the DPS signal as we have done in the analysis of $W \otimes jj$ and $Z \otimes jj$ channels. As only two visible charged leptons can be resolved, we need to consider their correlations to investigate the potential of measuring σ_{eff}.

We first examine the azimuthal angle distance $\Delta\phi$ of the two charged leptons. A rather flat distribution of $\Delta\phi(\ell_1, \ell_2)$ is expected for the $W^\pm \otimes W^\pm$ channel as the two charged leptons are completely independent in the DPS. Unfortunately, the SPS background also exhibits a nearly flat $\Delta\phi$ distribution such that the $\Delta\phi$ distribution is not suitable for measuring σ_{eff}.

Next, we consider the rapidity difference of the two charged leptons $\Delta\eta_{\ell\ell}$, defined as

$$\Delta\eta_{\ell\ell} = \eta_{\ell_1^\pm} - \eta_{\ell_2^\pm}, \qquad (40)$$

where $\ell_1^\pm$ denotes the leading p_T charged lepton and $\ell_2^\pm$ the subleading lepton. Figure 19 displays the magnitude of $\Delta\eta_{\ell\ell}$ distribution of the DPS signal (black) and the SPS background (blue). The DPS signal exhibits a more flatter distribution. The difference becomes more evident at the 100 TeV collider. Hence, one can measure the DPS signal through the rapidity difference of two charged leptons. The difference can be understood as follows. In the DPS subprocess of $d\bar{u} \to W^- \to \ell^- \bar{\nu}$, the charged lepton ℓ^- appears predominantly along the incoming d-quark direction, i.e.
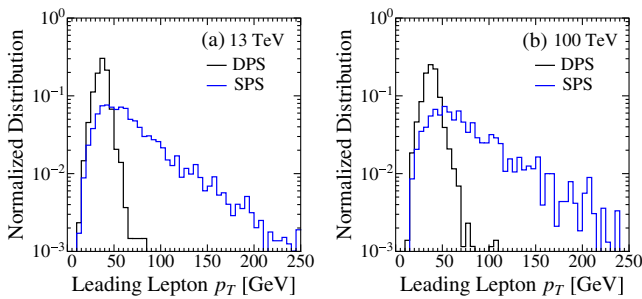

FIG. 18. The p_T distribution of the leading lepton in the $W^\pm \otimes W^\pm$ channel at the 13 TeV (a) and 100 TeV (b). The SPS background denotes the $W^\pm W^\pm jj$ production after vetoing additional jets as explained in text.
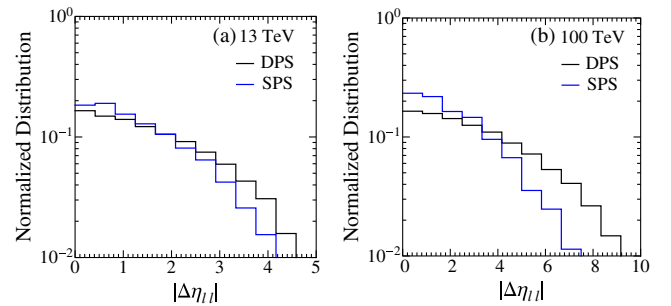

FIG. 19. The $|\Delta\eta_{\ell\ell}|$ distribution in the $W^\pm \otimes W^\pm$ channel at the 13 TeV (a) and 100 TeV collider (b). The SPS background denotes the $W^\pm W^\pm jj$ production after jet-veto.

$$\mathcal{M}(d_L \bar{u}_R \to W^- \to \ell_L^- \bar{\nu}_R) \propto \frac{1 + \cos\theta_{\ell d}}{2}, \quad (41)$$

where the $\theta_{\ell d}$ angle denotes the open angle between the charged lepton ℓ^- and the moving direction of the d-quark in the center of mass frame, i.e. $\cos\theta_{\ell d} \equiv \vec{p}_{\ell^-} \cdot \vec{p}_d / |\vec{p}_{\ell^-}||\vec{p}_d|$ with $\vec{p}_{\ell^-,d}$ being the charged lepton (d-quark) three-momentum defined in the center of mass frame. As a result, it is often that one of the two charged leptons appear in the forward region and the other in the backward region, just leading to a large rapidity gap. In the SPS background, the W-boson pairs tend to be produced in the central regions and their decay products often appear in the central region, yielding a small rapidity gap.

It is interesting to ask whether the $\Delta\eta_{\ell\ell}$ distribution is sensitive to the choice of dPDF. It has been pointed out in Ref. [39,69] that, the rapidity asymmetry of two charged leptons in the $W^\pm \otimes W^\pm$ DPS channel can manifest the difference of simple factorized dPDF and GS09 dPDF. The lepton rapidity asymmetry is defined as

$$\mathcal{A}_{\eta_\ell} = \frac{\sigma(\eta_{\ell_1} \times \eta_{\ell_2} < 0) - \sigma(\eta_{\ell_1} \times \eta_{\ell_2} > 0)}{\sigma(\eta_{\ell_1} \times \eta_{\ell_2} < 0) + \sigma(\eta_{\ell_1} \times \eta_{\ell_2} > 0)}. \quad (42)$$

The asymmetry is sensitive to the correlations between the two partons from one proton, which is described in Eq. (8) in the GS09 dPDF but absent in the simplified dPDF. As the correlation effect is evident in the large x region, a cut on the lepton rapidity ($|\eta_\ell| > \eta_{\min}^\ell$) could amplify the difference between those two dPDFs. Figure 20 shows the $\mathcal{A}_{\eta_\ell}$ distribution as a function of $\eta_{\min}^\ell$ at the 13 TeV LHC (a) and 100 TeV colliders (b). The 13 TeV result agrees well with Ref. [39]. In the SF dPDF, the two charged leptons are independent, yielding $\mathcal{A}_{\eta_\ell} \sim 0$ (see the blue points); in the GS09 dPDF, the two charged leptons tend to lie in different hemispheres with an axis defined by the beam line, giving rise to a positive $\mathcal{A}_{\eta_\ell}$ (see the black points). A much smaller x is reached at the 100 TeV colliders, thus weakening the difference between dPDFs.

In order to keep more DPS signal events, we do not impose the $\eta_{\min}^\ell$ cut, which is crucial to see the difference
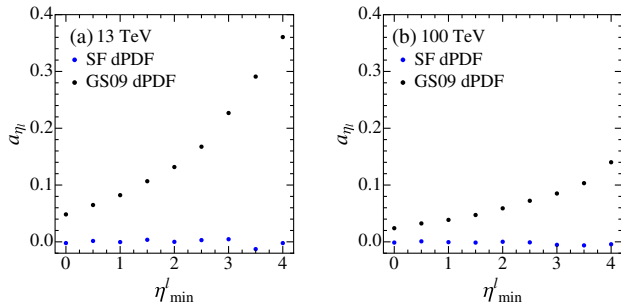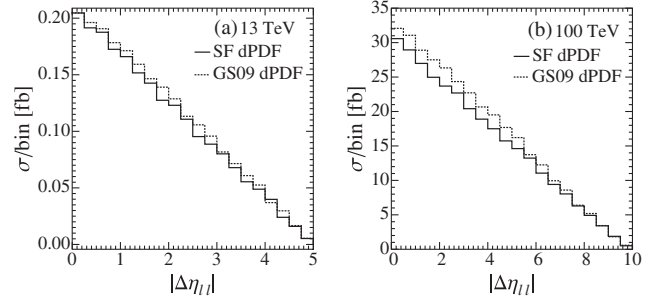

FIG. 21. The $\Delta\eta_{\ell\ell}$ distribution of two same-sign charged leptons calculated with different double parton distributions at the 13 TeV LHC (a) and the 100 TeV colliders (b).

between dPDFs. Therefore, the $|\Delta\eta_{\ell\ell}|$ distribution is not sensitive to the dPDF models in our analysis. Even though the SF and GS09 dPDFs produce a mild difference in the $|\Delta\eta_{\ell\ell}|$ distribution, it does not affect our fitting results, as Fig. 21 shows.

B. Collider simulation

The event topology of the $W^\pm \otimes W^\pm$ channel consists of two same-sign lepton and $\slashed{E}_T$. We also demand no hard jet activity. The major SPS backgrounds are (i) the $W^\pm W^\pm jj$ production with the two additional jets being vetoed, (ii) the $t\bar{t}$ pair production in which a charged lepton is generated from one top quark decay while another same-sign charged lepton arises from the bottom quark emitted from the other top, (iii) the $W^\pm Z/\gamma^*$ with $Z/\gamma^* \to \ell^+\ell^-$ and $W^\pm \to \ell^+\nu$; (iv) the $Z(\gamma^*)Z(\gamma^*) \to \ell^+\ell^-\ell^+\ell^-$ channel which is denoted as "$2\ell^+2\ell^-$". In order to suppress the SPS backgrounds, we choose five basic cuts listed below:

(1) Two same-sign charged leptons with $p_T^{\ell\pm} \geq 20$ GeV and $|\eta^{\ell\pm}| \leq 2.5$ at the 13 TeV LHC while $|\eta^{\ell\pm}| \leq 5$ at the 100 TeV SppC/FCC-hh;

(2) No hard jet with $p_T^j \geq 25$ GeV and $|\eta^j| \leq 2.5$ at the 13 TeV LHC while $p_T^j \geq 50$ GeV and $|\eta^j| \leq 5$ at the 100 TeV SppC/FCC-hh;

(3) $\slashed{E}_T \geq 20$ GeV;

(4) $M_{\ell_1^\pm \ell_2^\pm} \notin [75, 105]$ GeV;

(5) $p_T^{\ell\pm} < 60$ GeV.

Note that our lepton $p_T^{\ell\pm}$ cut is slightly different from Ref. [11], which introduces asymmetric cuts on the leading lepton and trailing lepton as $p_T^{\ell_1} > 20$ GeV and $p_T^{\ell_2} > 10$ GeV, respectively. In our analysis, we demand symmetric cuts on both leptons, $p_T^{\ell\pm} > 20$ GeV, which can suppress the WZ and $W\gamma^*$ backgrounds efficiently, Our simulation results are consistent with Ref. [39].

We choose the input value of $\sigma_{\rm eff} = 15$ mb and generate both the signal and background events in MadGraph with $p_T^j \geq 10$ GeV and $|\eta^j| < 5$. We further demand the charged leptons well separated in angular distance, i.e. $\Delta R_{\ell\ell} \geq 0.4$, in order to avoid the collinear divergence in the $\gamma^* \to \ell^+\ell^-$

FIG. 20. $\mathcal{A}_{\eta_\ell}$ versus $\eta_{\min}^\ell$ in SF and GS09 dPDFs at the 13 TeV LHC (a) and the 100 TeV colliders (b).

TABLE VII. Cross sections (in the unit of picobarn) of the $W^\pm \otimes W^\pm$ DPS signal process and the SM background process $W^\pm W^\pm jj$ at the 13 TeV LHC (top) and at the 100 TeV SppC/FCC-hh (bottom). The two additional jets in the background are rejected. We choose $\sigma_{\mathrm{eff}} = 15$ mb and impose the kinematic cuts listed in each column sequentially.

13 TeV	Gen.	Cut-1	Cut-2	Cut-3	Cut-4	Cut-5
$W^\pm \otimes W^\pm$	22.18	4.10	2.63	2.21	1.78	1.76
$W^\pm W^\pm jj$	71.98	11.78	0.64	0.58	0.47	0.19
$t\bar{t}$	461 001	0.64	0.00	0.00	0.00	0.00
WZ/γ^*	13 749.6	80.75	33.58	27.88	20.95	13.55
$2\ell^+ 2\ell^-$	749.94	10.47	5.25	0.88	0.69	0.43
100 TeV						
$W^\pm \otimes W^\pm$	1589.33	512.53	373.72	336.87	290.81	275.95
$W^\pm W^\pm jj$	1623.85	336.65	18.79	16.91	12.99	6.98
$t\bar{t}$	30 675 900	117.69	5.88	5.88	5.88	0.00
WZ/γ^*	85 482	1304.95	581.17	486.63	390.10	226.03
$2\ell^+ 2\ell^-$	5242.75	123.84	71.41	10.95	8.36	4.48

processes. We then pass the parton level events to Pythia for parton shower and merging. The cross section (in the unit of picobarn) of the signal and background processes after imposing the generator-level cuts are summarized in the second column of Table VII. Next, we adapt Delphes for particle identifications and then impose the four kinematics cuts. The last five columns in Table VII show the cross section after imposing the five basic cuts sequentially.

The identification of two same-sign charged leptons in the first cut (cut-1) is the most efficient cut to suppress the SPS backgrounds; see the third column in Table VII. While about 18% of the DPS signal events survive the cut-1, only 0.02% of the SPS background events remain. At the 100 TeV collider the lepton $|\eta^\ell|$ cut is extended to 5 in order to collect more signal events. We find that the lepton identification cut works better at the 100 TeV colliders; for example, about 0.006% of the SPS background events survive while about 32% of the DPS signal events remain. The jet-veto cut specified in the second cut (cut-2) is also very powerful in suppressing those backgrounds involving jets in the final state; see the fourth column. We introduce the $\not{E}_T$ cut (cut-3) to suppress the $2\ell^+ 2\ell^-$ backgrounds which do not have neutrinos at the parton level. Note that a potential background comes from the mistagging of multi-jet events. It has been shown by the CMS Collaboration [11] that such mistagged backgrounds can be efficiently suppressed by requiring the scalar sum of two charged leptons' p_T larger than 45 GeV, i.e. $p_T^{\ell_1} + p_T^{\ell_2} > 45$ GeV. Since we demand both the charged leptons exhibit $p_T^\ell > 20$ GeV in lepton trigger, the scalar sum condition is satisfied automatically. It is also possible that one of the two charged leptons from the Z boson decay is misidentified as opposite charged. It then provides a faked signal of two same-sign charged leptons. In the fourth cut (cut-4), we

demand the invariant mass of the same-sign lepton pair to be away from the Z boson resonance so as to remove those faked events, i.e. $|M_{\ell_1^\pm \ell_2^\pm} - m_Z| > 20$ GeV. Finally, we demand an upper bound on the charged lepton's p_T in the fifth cut (named as cut-5). Owing to the Jacobi peak feature of the W boson decay in the $W^\pm \otimes W^\pm$ DPS channel, the charged lepton exhibits a p_T mainly below ~ 40 GeV. The cut only mildly affects the DPS signal but sizably reduce the electroweak backgrounds.

After all the five basic cuts, the WZ/γ^* production becomes the dominant background. We end up with $f^{\mathrm{DPS}} = 11\%$ at the 13 TeV LHC and $f^{\mathrm{DPS}} = 54\%$ at the 100 TeV SppC/FCC-hh. Increasing collider energy improves the fraction f^{DPS} significantly.

C. Determining σ_{eff}

We perform a χ^2-fit of the $|\Delta\eta_{\ell\ell}|$ distribution, divided into 12 bins, to measure σ_{eff}. Figure 22 displays the $|\Delta\eta_{\ell\ell}|$ distributions of the DPS signal and the sum of all the SM backgrounds (labeled as background) after the five selection cuts. Note that the WZ/γ^* channel, not the $W^\pm W^\pm jj$ SPS background we examined, becomes the dominant background. The difference between the DPS signal and the SPS background we observed in Fig. 19 still remains. Figure 23 shows the $\sigma_{\mathrm{eff}}^{\mathrm{fit}}$ as a function of $\sigma_{\mathrm{eff}}^{\mathrm{input}}$ at the 13 TeV LHC (a) and 100 TeV colliders (b). The rate of the $W^\pm \otimes W^\pm$ DPS production is suppressed in comparison with the $W \otimes jj$ and $Z \otimes jj$ DPS channels. To study the impact of the statistical uncertainty on the fitting precision, we consider two benchmark luminosities in the fitting analysis: 300 fb^{-1} (red circle) and 3000 fb^{-1} (triangle). Two systematic errors, $f_{\mathrm{syst}} = 15\%$ and $f_{\mathrm{syst}} = 25\%$, are considered.

Due to the small rate of the $W^\pm \otimes W^\pm$ and large backgrounds ($f^{\mathrm{DPS}} = 11\%$) at the 13 TeV LHC, the accuracy of $\sigma_{\mathrm{eff}}^{\mathrm{fit}}$ is sensitive to the integrated luminosity. Upgrading the LHC to the phase of high luminosity, say $\mathcal{L} = 3000$ fb^{-1}, improves the fitting accuracy sizably; for example, see the circle and triangle points for each input $\sigma_{\mathrm{eff}}^{\mathrm{in}}$. At the 100 TeV collider, owing to the significant
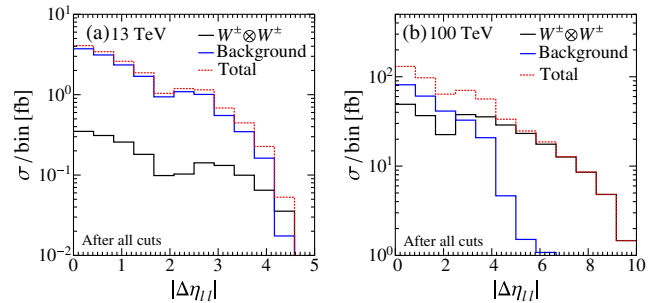

FIG. 22. The $|\Delta\eta_{\ell\ell}|$ distribution in the $W^\pm \otimes W^\pm$ channel after all of the five basic cuts at the 13 TeV (a) and 100 TeV (b).
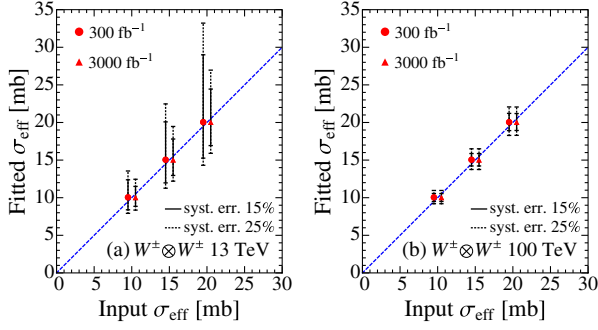
FIG. 23. The fitted σ_{eff} as a function of $\sigma_{\text{eff}}^{\text{in}}$ fitted in the $\Delta\eta_{\ell\ell}$ distribution at the 13 TeV (a) and 100 TeV colliders (b).

enhancement of the DPS production rate, the statistic uncertainty is well under control and the systematic error dominates the fitting precision. Therefore, accumulating more luminosity at the 100 TeV machine would not improve the accuracy of $\sigma_{\text{eff}}^{\text{fit}}$.

The fitted results for an integrated luminosity of 3000 fb^{-1} are as follows:

(i) $\sigma_{\text{eff}}^{\text{in}} = 10$ mb

$$\sigma_{\text{eff}}^{\text{fit}} = 10^{+1.50(+15.0\%)}_{-1.15(-11.5\%)}, \quad 10^{+2.45(+24.5\%)}_{-1.65(-16.5\%)}, \quad 13\,\text{TeV},$$

$$\sigma_{\text{eff}}^{\text{fit}} = 10^{+0.55(+5.5\%)}_{-0.50(-5.0\%)}, \quad 10^{+0.96(+9.6\%)}_{-0.80(-8.0\%)}, \quad 100\,\text{TeV};$$

(ii) $\sigma_{\text{eff}}^{\text{in}} = 15$ mb

$$\sigma_{\text{eff}}^{\text{fit}} = 15^{+2.80(+18.7\%)}_{-2.04(-13.6\%)}, \quad 15^{+4.47(+29.8\%)}_{-2.80(-18.7\%)}, \quad 13\,\text{TeV},$$

$$\sigma_{\text{eff}}^{\text{fit}} = 15^{+0.87(+5.8\%)}_{-0.78(-5.2\%)}, \quad 15^{+1.50(+10.0\%)}_{-1.25(-8.3\%)}, \quad 100\,\text{TeV};$$

(iii) $\sigma_{\text{eff}}^{\text{in}} = 20$ mb,

$$\sigma_{\text{eff}}^{\text{fit}} = 20^{+4.44(+22.2\%)}_{-3.07(-15.4\%)}, \quad 20^{+6.96(+34.8\%)}_{-4.10(-20.5\%)}, \quad 13\,\text{TeV},$$

$$\sigma_{\text{eff}}^{\text{fit}} = 20^{+1.19(+6.0\%)}_{-1.06(-5.3\%)}, \quad 20^{+2.06(+10.3\%)}_{-1.71(-8.6\%)}, \quad 100\,\text{TeV},$$

where the first value of $\sigma_{\text{eff}}^{\text{fit}}$ is for $f_{\text{syst}} = 15\%$ while the second value for $f_{\text{syst}} = 25\%$. The superscript and subscript denotes the upper and lower error and the percentage denotes the fraction of the error normalized to the mean value of $\sigma_{\text{eff}}^{\text{fit}}$.

VII. DISCUSSION AND CONCLUSIONS

In the LHC era, with much higher collision energies available, DPS has received several experimental and theoretical studies. Lacking theoretical ground, the phenomenological studies are based on the factorized ansatz of the double parton distribution functions, which neglect momentum correlations between partons and introduce an effective cross section σ_{eff}. The latter quantity is to be extracted from experimental data and might vary for

different processes. As σ_{eff} is connected with the effective size of the hard scattering core of the proton, the variation in the values of σ_{eff} may mean that σ_{eff} will have different values for qq, qg, and $q\bar{q}$ scatterings. It is desirable to establish double parton scattering in data and determine σ_{eff} in a relatively clean processes. In this work, we demonstrate that the DPS production involving weak gauge bosons is important for measuring σ_{eff} because the leptons from the W and Z boson decays provide a nice trigger of the DPS signal. Specifically, we focus on the $W \otimes jj$, $Z \otimes jj$ and $W^{\pm} \otimes W^{\pm}$ channels and explore the potential of measuring σ_{eff} at the 13 and 100 TeV proton-proton colliders.

Several observables characterizing the feature of DPS have been proposed to optimize the DPS signal in the literature [49,50]. Our study shows that the best observable to measure σ_{eff} is: the relative p_T balance of jets ($\Delta^{\text{rel}} p_T$) in $W \otimes jj$, the relative p_T balance of leptons ($\Delta_{\ell}^{\text{rel}} p_T$) in $Z \otimes jj$, and $\Delta\eta_{\ell\ell}$ in $W^{\pm} \otimes W^{\pm}$. Note that $\Delta_{\ell}^{\text{rel}} p_T$ works better than $\Delta_{j}^{\text{rel}} p_T$ in $Z \otimes jj$. Taking advantage of those optimal observables, we show that it is very promising to observe the DPS signal on top of the SPS backgrounds. Figure 24(a) displays the fraction of the DPS signal event in the total event collected (f^{DPS}), defined in Eq. (27), after imposing the optimal cuts specified in main text. At the 13 TeV LHC, $f^{\text{DPS}}(W \otimes jj) \sim 34\%$, $f^{\text{DPS}}(Z \otimes jj) \sim 45\%$, and $f^{\text{DPS}}(W^{\pm} \otimes W^{\pm}) \sim 10\%$; at the 100 TeV colliders, f^{DPS} increases dramatically, say $f^{\text{DPS}}(W \otimes jj) \sim 45\%$, $f^{\text{DPS}}(Z \otimes jj) \sim 78\%$, and $f^{\text{DPS}}(W^{\pm} \otimes W^{\pm}) \sim 54\%$, owing to the huge enhancement of the production rate of the DPS processes.

Once double parton scattering is established in the data and σ_{eff} is determined, one can address the three questions raised in Sec. I: (i) how well can one measure σ_{eff}? (ii) does σ_{eff} vary with colliding energies? (iii) is σ_{eff} universal for various DPS processes?

Figure 24(b) displays the recent experimental data (left panel) and the projected accuracies of σ_{eff} measurement obtained from our collider simulations with the choice of $\sigma_{\text{eff}}^{\text{in}} = 15$ mb (right panel). The recent experimental data are summarized in Table II, which suggests an average value of $\sigma_{\text{eff}} \simeq 15$ mb. For the three DPS channels of interest to us, the red (blue) points denote the $\sigma_{\text{eff}}^{\text{fit}}$ obtained at the 13 (100) TeV colliders, respectively. The $W \otimes jj$ and $Z \otimes jj$ channels are able to measure the σ_{eff} with errors less than the current data, assuming the systematic error is 15% or 25%. Since the uncertainties of the two DPS channels are dominated by the systematic errors, we present the fitting results with an integrated luminosity of 300 fb^{-1}. Note that accumulating more luminosity cannot improve the accuracy. At the 100 TeV colliders, the DPS production rate increases dramatically such that the σ_{eff} measurement can be sizably improved.

The $Z \otimes jj$ channel gives a better precision than the $W \otimes jj$ channel; for example, assuming a 15% systematic
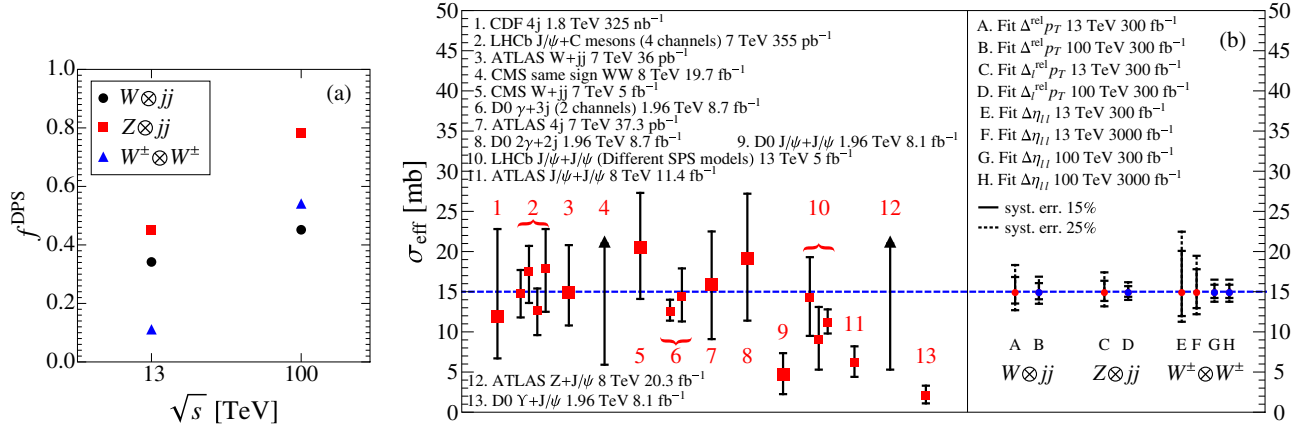
FIG. 24. (a) f^{DPS} (the fraction of the DPS signal events in the total events) in the three DPS processes after the optimal cuts at the 13 and 100 TeV colliders. (b) Recent experimental data of σ_{eff} measurement (left) and the projected $\sigma_{\mathrm{eff}}^{\mathrm{fit}}$ in the $W \otimes jj$, $Z \otimes jj$ and $W^{\pm} \otimes W^{\pm}$ channels (right).

error, one can measure the σ_{eff} through the $\Delta_{\ell}^{\mathrm{rel}} p_T$ distribution with a precision as

$$\sigma_{\mathrm{eff}}^{\mathrm{fit}}(W \otimes jj) = 15^{+1.83(+12.2\%)}_{-1.47(-9.8\%)},$$

$$\sigma_{\mathrm{eff}}^{\mathrm{fit}}(Z \otimes jj) = 15^{+1.36(+9.1\%)}_{-1.15(-7.7\%)},$$

at the 13 TeV LHC, and

$$\sigma_{\mathrm{eff}}^{\mathrm{fit}}(W \otimes jj) = 15^{+1.07(+7.1\%)}_{-0.94(-6.3\%)},$$

$$\sigma_{\mathrm{eff}}^{\mathrm{fit}}(Z \otimes jj) = 15^{+0.69(+4.6\%)}_{-0.63(-4.2\%)},$$

at the 100 TeV colliders with an integrated luminosity of 300 fb^{-1}. See the points A, B, C, and D in Fig. 24(b). Therefore, we argue that one should explore the $Z \otimes jj$ channel to measure σ_{eff}.

The $W^{\pm} \otimes W^{\pm}$ channel has been studied extensively in the literature for the reason that it has a clean signature of two charged leptons and large missing transverse momentum. However, the channel suffers from small production rate and lack of distinctive observables discriminating the DPS signal from the SPS backgrounds. Therefore, the uncertainty of σ_{eff} measurements is worse than that of the $W \otimes jj$ and $Z \otimes jj$ channels. For the same reason, the recent CMS measurement provides only a lower limit of σ_{eff}; see the fourth data in the left panel of Fig. 24(b). Though suffering from large uncertainties, the $W^{\pm} \otimes W^{\pm}$ signal can be measured in the $|\Delta\eta_{\ell\ell}|$ distribution at the 13 TeV LHC, and the accuracy can be further improved at the high luminosity phase. For example, choosing an input $\sigma_{\mathrm{eff}}^{\mathrm{in}} = 15$ mb and assuming a 15% systematic error, one can measure σ_{eff} through the $\Delta\eta_{\ell\ell}$ distribution with a precision as $15^{+5.08(+33.9\%)}_{-3.03(-20.2\%)}$ and $15^{+2.80(+18.7\%)}_{-2.04(-13.6\%)}$ with an integrated luminosity of 300 fb^{-1} and 3000 fb^{-1}, respectively; see the points E and F in Fig. 24(b). At the 100 TeV

colliders, the DPS signal rate dominates over the SPS background, thus leading to a much better precision $15^{+0.87(+5.8\%)}_{-0.78(-5.2\%)}$ with an integrated luminosity of ≥ 300 fb^{-1}; see the points G and H in Fig. 24(b). With the projected accuracy, one might be able to check whether σ_{eff} varies with the colliding energy.

Now check the universality of σ_{eff} for different DPS processes. The current data imply $\sigma_{\mathrm{eff}} \sim 15$ mb but with large uncertainties. Figure 25 shows the correlations among the $\sigma_{\mathrm{eff}}^{\mathrm{fit}}$'s measured in the three DPS channels: (a)–(b) $Z \otimes jj$ versus $W \otimes jj$, (c)–(d) $W^{\pm} \otimes W^{\pm}$ versus $W \otimes jj$. The yellow and green bands represent the region of a universal σ_{eff} at the 1σ level with a systematic error of 15% and 25%, respectively. Any data falling outside the band indicate that σ_{eff} is process dependent. The weak boson productions are sensitive to the flavor of quarks inside proton. As shown in Sec. III C, the DPS channels we considered depend mainly on parton combinations listed as follows:

$$W \otimes jj: \sigma_{\mathrm{eff}}(qg \otimes \bar{q}'g),$$

$$Z \otimes jj: \sigma_{\mathrm{eff}}(qg \otimes \bar{q}g),$$

$$W^{\pm} \otimes W^{\pm}: \sigma_{\mathrm{eff}}(u\bar{d} \otimes u\bar{d}), \sigma_{\mathrm{eff}}(qq \otimes \bar{q}'\bar{q}').$$

A process-dependent σ_{eff} means that the σ_{eff} will have different values for qq, qg, and $q\bar{q}$ scatterings. Note that our theory calculation is based on the assumption that the $F(b)$ function is universal for any two partons in one proton. Deviation from the yellow or green band might indicate that the assumption of a universal function $F(b)$ is not valid.

Note that the uncertainty bands in the correlation between $W \otimes jj$ and $Z \otimes jj$, shown in Figs. 25(a) and 25(b), are dominated by the systematic errors. We plot the 1σ bands with an integrated luminosity of 300 fb^{-1}, and increasing luminosity will not alter the band width. The $W^{\pm} \otimes W^{\pm}$ channel has a large statistical uncertainty in the
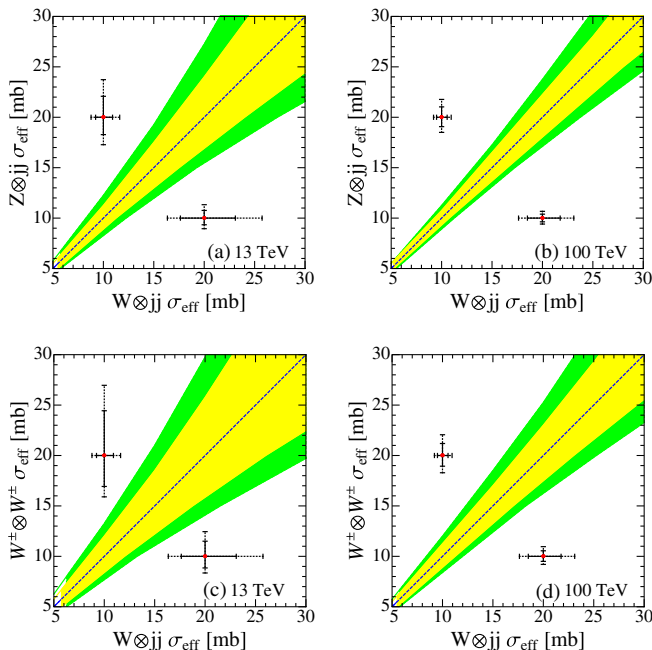
FIG. 25. Universality check of $\sigma_{\text{eff}}^{\text{fit}}$: (a)–(b) $Z \otimes jj$ versus $W \otimes jj$ with $\mathcal{L} \geq 300$ fb^{-1}, (c)–(d) $W^{\pm} \otimes W^{\pm}$ versus $W \otimes jj$ with $\mathcal{L} = 3000$ fb^{-1}. The yellow (green) band denotes the region of a universal σ_{eff} at the 1σ confidence level with a systematic error of 15% (25%), respectively.

σ_{eff} measurement, therefore, it requires a high luminosity to make $W^{\pm} \otimes W^{\pm}$ usable. We obtain the 1σ bands in Figs. 25(c) and 25(d) using an integrated luminosity of 3000 fb^{-1}. One is able to test the σ_{eff} universality if the σ_{eff}'s of two different DPS processes are not too close. For example, $\sigma_{\text{eff}}(W \otimes jj) = 10$ mb and $\sigma_{\text{eff}}(Z \otimes jj) = 20$ mb can be well distinguished at the 13 TeV LHC. A better test of σ_{eff} universality is expected at the 100 TeV colliders. It is worth mentioning that one should also take the $\gamma j \otimes jj$ channel into account for a better and comprehensive comparison.

In short, we affirm that the double parton scattering processes involving weak bosons ($W \otimes jj$, $Z \otimes jj$, and $W^{\pm} \otimes W^{\pm}$) are promising at the LHC and future hadron colliders. The $Z \otimes jj$ channel is the best in measuring the effective cross section σ_{eff}. Once DPS is established in data and σ_{eff} is determined, one can test the universality of σ_{eff} in the three channels.

ACKNOWLEDGMENTS

[1] CEPC-SPPC Study Group, CEPC-SPPC Preliminary Conceptual Design Report. 1. Physics and Detector, Report No. IHEP-CEPC-DR-2015-01, 2015.

[2] M. Mangano, Physics at the FCC-hh, a 100 TeV pp collider, CERN Yellow Report No. CERN 2017-003-M.

[3] M. Aaboud *et al.* (ATLAS Collaboration), J. High Energy Phys. 11 (2016) 110.

[4] F. Abe *et al.* (CDF Collaboration), Phys. Rev. D **47,** 4857 (1993).

[5] ATLAS Collaboration, CERN, Technical Report ATLAS-CONF-2015-058, 2015, http://cds.cern.ch/record/2108894.

[6] T. Akesson *et al.* (Axial Field Spectrometer Collaboration), Z. Phys. C **34,** 163 (1987).

[7] J. Alitti *et al.* (UA2 Collaboration), Phys. Lett. B **268,** 145 (1991).

[8] R. Kumar, S. Bansal, M. Bansal, V. Bhatnagar, K. Mazumdar, and J. B. Singh, Springer Proc. Phys. **174,** 147 (2016).

[9] S. Chatrchyan *et al.* (CMS Collaboration), J. High Energy Phys. 03 (2014) 032.

[10] G. Aad *et al.* (ATLAS Collaboration), New J. Phys. **15,** 033038 (2013).

[11] CMS Collaboration, CERN, Technical Report CMS-PAS-FSQ-13-001, 2015, https://cds.cern.ch/record/2103756.

[12] M. Myska, in *Proceedings of Physics at LHC 2011, Perugia, Italy, 2011* (2012), arXiv:1206.4427.

[13] M. Myska, Ph.D. thesis, Prague Technical University, 2013, https://inspirehep.net/record/1296576/files/696873160_CERN-THESIS-2013-058.pdf.

[14] CMS Collaboration, CERN, Technical Report CMS-PAS-FSQ-16-009, 2017, http://cds.cern.ch/record/2257583.

[15] C. H. Kom, A. Kulesza, and W. J. Stirling, Phys. Rev. Lett. **107,** 082002 (2011).

[16] S. P. Baranov, A. M. Snigirev, and N. P. Zotov, Phys. Lett. B **705,** 116 (2011).

[17] A. Novoselov, arXiv:1106.2184.

[18] M. Luszczak, R. Maciula, and A. Szczurek, Phys. Rev. D **85,** 094034 (2012).

[19] R. Maciula and A. Szczurek, Phys. Rev. D **96,** 074013 (2017).

[20] J.-P. Lansberg, H.-S. Shao, and N. Yamanaka, arXiv:1707.04350.

[21] C. Borschensky and A. Kulesza, Phys. Rev. D **95,** 034029 (2017).

[22] J.-P. Lansberg and H.-S. Shao, Nucl. Phys. **B916,** 132 (2017).

[23] J.-P. Lansberg and H.-S. Shao, Phys. Lett. B **751,** 479 (2015).

[24] R. Aaij *et al.* (LHCb Collaboration), J. High Energy Phys. 06 (2012) 141; 03 (2014) 108(A).

[25] V. M. Abazov *et al.* (D0 Collaboration), Phys. Rev. D **90,** 111101 (2014).

[26] R. Aaij *et al.* (LHCb Collaboration), J. High Energy Phys. 06 (2017) 047; 10 (2017) 068.

[27] M. Aaboud *et al.* (ATLAS Collaboration), Eur. Phys. J. C **77,** 76 (2017).

[28] G. Aad *et al.* (ATLAS Collaboration), J. High Energy Phys. 04 (2014) 172.

[29] G. Aad *et al.* (ATLAS Collaboration), Eur. Phys. J. C **75,** 229 (2015).

[30] V. M. Abazov *et al.* (D0 Collaboration), Phys. Rev. Lett. **116,** 082002 (2016).

[31] J.-P. Lansberg and H.-S. Shao, Phys. Rev. Lett. **111,** 122001 (2013).

[32] Y.-J. Li, G.-Z. Xu, K.-Y. Liu, and Y.-J. Zhang, J. High Energy Phys. 07 (2013) 051.

[33] L.-P. Sun, H. Han, and K.-T. Chao, Phys. Rev. D **94,** 074033 (2016).

[34] J.-P. Lansberg and H.-S. Shao, J. High Energy Phys. 10 (2016) 153.

[35] H.-S. Shao and Y.-J. Zhang, Phys. Rev. Lett. **117,** 062001 (2016).

[36] V. M. Abazov *et al.* (D0 Collaboration), Phys. Rev. D **89,** 072006 (2014).

[37] V. M. Abazov *et al.* (D0 Collaboration), Phys. Rev. D **93,** 052008 (2016).

[38] J. C. Collins, D. E. Soper, and G. F. Sterman, Adv. Ser. Dir. High Energy Phys. **5,** 1 (1989).

[39] J. R. Gaunt, C.-H. Kom, A. Kulesza, and W. J. Stirling, Eur. Phys. J. C **69,** 53 (2010).

[40] J. R. Gaunt and W. J. Stirling, J. High Energy Phys. 03 (2010) 005.

[41] M. Rinaldi, S. Scopetta, M. Traini, and V. Vento, J. High Energy Phys. 12 (2014) 028.

[42] M. Rinaldi, S. Scopetta, M. Traini, and V. Vento, Phys. Lett. B **752,** 40 (2016).

[43] M. Traini, M. Rinaldi, S. Scopetta, and V. Vento, Phys. Lett. B **768,** 270 (2017).

[44] A. M. Snigirev, Phys. Rev. D **68,** 114012 (2003).

[45] V. L. Korotkikh and A. M. Snigirev, Phys. Lett. B **594,** 171 (2004).

[46] M. Rinaldi and F. A. Ceccopieri, Phys. Rev. D **95,** 034040 (2017).

[47] K. Golec-Biernat and A. M. Stasto, Phys. Rev. D **95,** 034033 (2017).

[48] E. Maina, J. High Energy Phys. 01 (2011) 061.

[49] E. L. Berger, C. B. Jackson, and G. Shaughnessy, Phys. Rev. D **81,** 014014 (2010).

[50] E. L. Berger, C. B. Jackson, S. Quackenbush, and G. Shaughnessy, Phys. Rev. D **84,** 074021 (2011).

[51] M. Y. Hussein, in *SUSY 2007 proceedings, 15th International Conference on Supersymmetry and Unification of Fundamental Interactions, 2007, Karlsruhe, Germany* (2007), http://www.susy07.uni-karlsruhe.de/Proceedings/proceedings/susy07.pdf.

[52] R. M. Godbole, S. Gupta, and J. Lindfors, Z. Phys. C **47,** 69 (1990).

[53] B. Blok and P. Gunnellini, Eur. Phys. J. C **76,** 202 (2016).

[54] A. Del Fabbro and D. Treleani, Phys. Rev. D **61,** 077502 (2000).

[55] D. Bandurin, G. Golovanov, and N. Skachkov, J. High Energy Phys. 04 (2011) 054.

[56] E. Maina, J. High Energy Phys. 09 (2009) 081.

[57] A. Kulesza and W. J. Stirling, Phys. Lett. B **475,** 168 (2000).

[58] C. Quigg, arXiv:0908.3660.

[59] A. D. Martin, W. J. Stirling, R. S. Thorne, and G. Watt, Eur. Phys. J. C **63,** 189 (2009).

[60] Airapetian *et al.* (ATLAS Collaboration), *ATLAS Detector and Physics Performance: Technical Design Report, 1*, Technical Design Report ATLAS (CERN, Geneva, 1999), http://cds.cern.ch/record/391176.

[61] Bayatian *et al.* (CMS Collaboration), *CMS Physics: Technical Design Report Volume 1: Detector Performance and Software*, Technical Design Report CMS (CERN, Geneva, 2006), http://cds.cern.ch/record/922757.

[62] M. L. Mangano *et al.*, CERN, Yellow Report No. 3, 2017.

[63] J. Alwall, R. Frederix, S. Frixione, V. Hirschi, F. Maltoni, O. Mattelaer, H. S. Shao, T. Stelzer, P. Torrielli, and M. Zaro, J. High Energy Phys. 07 (**2014**) 079.

[64] T. Sjostrand, S. Mrenna, and P. Z. Skands, J. High Energy Phys. 05 (2006) 026.

[65] J. de Favereau, C. Delaere, P. Demin, A. Giammanco, V. Lematre, A. Mertens, and M. Selvaggi (DELPHES 3 Collaboration), J. High Energy Phys. 02 (2014) 057.

[66] C. Balazs and C. P. Yuan, Phys. Rev. D **56,** 5558 (1997).

[67] Q.-H. Cao and C. P. Yuan, Phys. Rev. Lett. **93,** 042001 (2004).

[68] ATLAS Collaboration, CERN, Technical Report ATLAS-CONF-2016-046, 2016, http://cds.cern.ch/record/2206128.

[69] F. A. Ceccopieri, M. Rinaldi, and S. Scopetta, Phys. Rev. D **95,** 114030 (2017).

[70] R. Schwienhorst, C. P. Yuan, C. Mueller, and Q.-H. Cao, Phys. Rev. D **83,** 034019 (2011).

[71] E. L. Berger, Q.-H. Cao, C.-R. Chen, C. S. Li, and H. Zhang, Phys. Rev. Lett. **106,** 201801 (2011).

[72] E. L. Berger, Q.-H. Cao, C.-R. Chen, G. Shaughnessy, and H. Zhang, Phys. Rev. Lett. **105,** 181802 (2010).